Journal of the Mechanics and Physics of Solids 125 (2019) 225–254

Contents lists available at ScienceDirect

Journal of the Mechanics and Physics of Solids

journal homepage: www.elsevier.com/locate/jmps

Simultaneous extraction of tensile and shear interactions at interfaces

Chenglin Wu[a,b], Rui Huang[a], Kenneth M. Liechti[a,*]

[a] Research Center for the Mechanics of Materials, Solids and Structures, Department of Aerospace Engineering and Engineering Mechanics University of Texas, Austin, TX 78712, United States

[b] Department of Civil, Architectural, and Environmental Engineering, Missouri University of Science and Technology, Rolla, MO 65409, United States

ARTICLE INFO

Article history:
Received 9 May 2018
Revised 22 September 2018
Accepted 4 December 2018
Available online 12 December 2018

Keywords:
Cohesive zone modeling
Interfacial interactions
Mixed-mode fracture
Traction–separation relations

ABSTRACT

A simple beam analysis is developed that accounts for the tensile and shear interactions between the surfaces of two beams that have been brought into contact. The generally coupled differential equations for the relative normal and tangential displacements between the interacting surfaces and the normal and shear components of the traction between the two surfaces are decoupled when a balance condition involving the bending stiffness and height of each beam is satisfied. This condition also allows the normal and shear components of the J-integral and the crack tip displacement to be obtained from measurements of the applied loads along with load point displacement and rotation of each beam. As a result, the derivative of each component of the J-integral with respect to its associated crack tip displacement simultaneously provides both the normal and shear traction–separation relations at any value of the mode-mix without invoking any assumption on the particular form. As an application of this method, the normal and shear traction–separation relations for a silicon/epoxy interface were determined over nominal mode-mixes ranging from −53° to 87.5° using non-symmetric end-loaded split (ELS) and end-notched flexure (ENF) specimens. It is found that many of the assumptions made previously in developing traction–separation relations based on potential or damage-based approaches do not apply to this particular interface, which should motivate future theoretical developments.

1. Introduction

Interfacial fracture in multi-layer structures has been a critical issue for thin film/substrate systems in electronic packages (Ho et al., 2004; Liu et al., 2007). Especially in integrated chip-package systems, interfacial fractures along die and die-attach, die and epoxy molding compound interfaces are commonly observed after thermal processing (Zhang et al., 2008). Interfacial fracture is also important in nanomanufacturing where it can be exploited for selective delamination in transfer printing (Kim-Lee et al., 2014; Carlson et al., 2011) and roll-to-roll processes (Na et al., 2015; Xin et al., 2017). These interfacial fractures normally propagate under mixed-mode conditions due to differences in material properties, layer thicknesses, residual stresses as well as the globally applied loading conditions. In what follows, we briefly review developments in mod-

* Corresponding author.
E-mail address: kml@mail.utexas.edu (K.M. Liechti).

https://doi.org/10.1016/j.jmps.2018.12.004
0022-5096/

eling and experiments for interfacial fracture, focusing on cohesive zone models and experimental methods for extracting traction–separation relations.

1.1. Cohesive zone modeling

The analysis of crack growth at interfaces was initially approached from what has become known as the linearly elastic fracture mechanics (LEFM) approach (Hutchinson and Suo, 1992). It is often used when brittle fracture conditions prevail in situations where the fracture process zone is small and the materials are elastic. For larger fracture process zones, the nonlinear behavior of the interactions just ahead of the crack front is accounted for by the cohesive zone modeling approach, which is able to simulate the development of the fracture process or cohesive zone along the interface.

The cohesive zone modeling approach was first proposed for monolithic materials by Dugdale (1960) and Barrenblatt (1962) in order to describe the fracture processes in metals by accounting for plasticity near the crack tip. Needleman (1987) and Ungsuwarungsri and Knauss (1987) first applied this approach in modeling interfacial crack propagation. By introducing traction–separation relations to represent interfacial interactions, this approach offered a way to model the nucleation and propagation of interfacial cracks, something that is lacking in LEFM analyses. Cohesive zone modeling soon became popular not only for modeling interfacial delamination (Feraren and Jensen, 2004; Li et al., 2005; Parmigiani and Thouless, 2007; Valoroso and Champaney, 2006), but also for other interface problems such as crack nucleation at bi-material corners (Mohammed and Liechti, 2000), plastic dissipation in thin films (Shirani and Liechti, 1998), and delamination of composites (Sørensen and Jacobsen, 2003; Li and Thouless, 2006; Moroni and Pirondi, 2011). However, specific interfacial traction–separation relations are required to properly describe the fracture process and make meaningful predictions. In addition, because interfacial fracture generally involves combinations of tension and shear interactions at the interface or mixed-mode effects, both normal and shear traction–separation relations are required and they are coupled in general (Li et al., 2006; Högberg et al., 2007; Parmigiani and Thouless, 2007; Zhu et al., 2009).

In the early development of the cohesive zone modeling approach, the form of traction–separation relations was often assumed. In the simplest case, the traction is constant over entire interaction range (Dugdale, 1960; Barenblatt, 1962). The trapezoidal and the bilinear forms of traction–separation relations were later assumed as a more realistic description of the failing material with softening interactions ahead of the crack front (Tvergaard and Hutchinson, 1996). Other forms of traction–separation relations have been assumed, representing different fracture mechanisms. However, the following characteristics are generally observed (Park et al., 2009): (1) the traction–separation relations are independent of superimposed rigid body motion; (2) the fracture energy defined as the area under the traction–separation relation is finite; (3) the mode-I (tensile) and mode-II (shear) fracture energies generally differ; (4) critical separations exist which lead to zero tractions; (5) softening stages exist; (6) a potential energy function for the traction–separation relations may or may not exist.

Based on observation (6), traction–separation relations can be categorized as potential-based or damage-based. The most commonly implemented potential-based traction–separation relations are the ones developed by Xu and Needleman (1993) in which traction–separation relationships are obtained from the first derivatives of an interface potential function. In this model, normal and shear interactions are coupled via exponentially decaying functions of normal and tangential separation (McGarry et al., 2014). The ratio of the work of tangential separation to the work of normal separation was defined to determine the strength of interface under mode I and mode II separation. Although this ratio varied for a number of interfaces (Dollhofer et al., 2000; Warrior et al., 2003; Yang et al., 2001), it has often been taken as a constant in many implementations (Rahulkumar et al., 2000; Yuan and Chen, 2003; Zavattieri et al., 2008). In the potential-based model, the absence of damage means that there is no energy dissipation during loading–unloading cycles. This is not only potentially an issue whenever the loading protocol is non-monotonic, but it also means that the interfacial interactions are reversible and do not dissipate energy during crack growth. In the damage-based traction–separation relations, the decaying portion of the traction–separation relation is often associated with a damage factor, which is a function of the vectorial separation (Ungsuwarungsru and Knauss, 1987; Alfano and Crisfield, 2001). The damage factor penalizes the stiffness to simulate the softening behavior of the interface. The coupling of the normal and shear interactions is often established by a shared damage factor. In damage-based models, energy dissipation exists due to the aforementioned stiffness penalty during damage evolution and is irreversible.

1.2. Extracting traction–separation relations

The determination of traction–separation relations may be approached either directly or iteratively. In the direct approach, the specific mode-mix is identified using a linear elastic fracture mechanics analysis prior to the extraction of traction–separation relations. The J-integral is then calculated approximately using analytical solutions. The local crack tip deformations are measured and the traction–separation relations can then be obtained directly by taking the derivative of the J-integral with respect to the measured crack tip displacements. This method has been demonstrated by many groups (Stigh and Andersson, 2000; Sørensen and Jacobsen, 2003; Andersson and Stigh, 2004; Sorensen et al., 2008; Zhu et al., 2009; Gowrishankar et al., 2012). On the other hand, the iterative approach determines the parameters associated with assumed functional forms of traction–separation relations by comparing numerical solutions of variables such as load, crack extension (resistance curves), crack opening displacements, etc. to measurements. By matching the local measurements to

cohesive zone modeling results (Cox and Marshall, 1991; Swadener and Liechti, 1998; Mohammed and Liechti, 2000; Li et al., 2005; Li et al., 2010; Mello and Liechti, 2006; Sørensen et al., 2008; Gain et al., 2011; Shen and Paulino, 2011; Na et al., 2015) or by comparing far-field measurements such as load–displacement response, specific traction–separation relations are extracted at any particular mode-mix.

The extraction of traction–separation relations by relying on only far-field measurements is essentially an inverse problem, which can be categorized into two types. In the first type, the extraction uses whole-field deformation measurements such as moiré interferometry (Guo et al., 1999; Mohammed and Liechti, 2000). The second type uses measured load–displacement or resistance curve data to find the optimal parameters for the traction–separation relations.

The first approach is based on the Almansi theorem of elasticity (Sokolnikoff, 1946), which states that if the displacements and tractions are simultaneously prescribed over a finite region of the boundary of an elastic body, the whole elastic field is then uniquely determined. As an example of this approach, Hong and Kim (2003) and Kim et al. (2012) developed the field projection method to extract the traction–separation relations from full-field measurements. In this inversion analysis, a solution method was developed that utilizes the path-independent interaction J-integral applied to an eigenfunction expansion of the cohesive crack-tip field. First, a fundamental elastic-field solution to a semi-infinite crack with a cohesive zone is developed, which was used as an auxiliary probe field. By applying interaction J-integrals between the auxiliary field and the measured displacement data, the coefficients of the eigenfunction expansion are then determined. This method ensures the uniqueness of the extracted traction–separation relations, thereby providing a powerful tool for extracting traction–separation relations under mixed-mode conditions.

The second approach is commonly applied to laminated beam type specimens, where the path-independent J-integral can be estimated through beam theories or finite element analysis. A functional form of the traction–separation relations is usually assumed depending on the material systems and the corresponding fracture processes. Then the parameters of the assumed functional form are found iteratively by optimizing the parameters to match the numerical results obtained using finite element analysis to measured data. However, any coupling between the normal and shear tractions along the interface makes this process difficult.

Nguyen and Levey (2009) presented an exact theory of interfacial debonding in layered elastic composites using Fourier series. In their model, interfacial interactions were captured by non-linear springs. Wang et al. (2013) developed expressions for energy release rates in layered isotropic double cantilever beams with non-rigid cohesive interfaces. Conroy et al. (2015) conducted mixed-mode experiments and pointed out that the traction distribution in the cohesive zone is dependent on the coupling of the governing equations for the variation of separation along the interface. Ouyang and Li (2009) reported on the decoupling of tension and shear interactions in the governing equation for the shear traction distribution in the end-notched flexure experiment and conducted experiments for extracting interfacial properties in pure Mode-II and moderate mode-mixes by varying the thickness of the adhesive (Ji et al., 2012). In their work, the single leg bending configuration was used. The range of mode-mix was limited because both adherends were made of the same material and had the same thickness. The relationship between the local crack tip displacements and measurements of global parameters such as load and load-line displacement and rotation was not revealed. As a result, the local crack-tip opening displacements (CTODs) were measured from images captured near the crack tip using a CCD camera. The resolution of the local CTOD measurements was about 3.7 μm/pixel, which caused challenges for silicon/epoxy interfaces where critical separations are normally on the order of several μm (Gowrishankar et al., 2012; Wu et al., 2016). In this work, we exploit the decoupling concept of Ouyang and Li (2009) for determining the normal and shear components of traction–separation relations at any mode-mix.

1.3. Loading configurations

The symmetric double cantilever beam (DCB) specimen (Kanninen, 1973; Chow et al., 1979; Williams, 1989; Zhu et al., 2009) has been mainly used for characterizing tensile interfacial interactions (mode I). Mixed-mode interactions have been obtained by introducing asymmetries in the geometry or loading (Sørensen and Kirkegaard, 2006; Mangalgiri et al., 1986; Sundararaman and Davidson, 1997). Other commonly used mixed-mode specimens include the four-point bend test (Charalambides et al., 1989; Charalambides et al., 1990) and the end loaded split (Hutchinson and Suo, 1992; Wang and Vukanh, 1996). The nature of mixed-mode experiments has always required the need for innovation which has brought about a lot of modifications to previously existing mixed-mode test specimens (Reeder and Crews Jr., 1990; Fernlund and Spelt, 1994; Sundararaman and Davidson, 1997; Sorensen et al., 2006; Bing and Davidson, 2010). Each specimen however has its own advantages and limitations with respect to the mode-mix range provided, the material system dependence and the ease of implementation.

As mentioned earlier, local crack tip measurements such as crack front location and opening are often required for the extraction of traction–separation relations. Crack opening interferometry (Liechti, 1993), digital image correlation (Pan et al., 2009), and laser generated stress pulses (Pronin and Gupta, 1998) have been developed in the past decade to provide such measurements. Crack opening interferometry has been used to characterize crack tip behavior in glass/adhesive systems (Chai and Liechti, 1992; Liechti, 1993; Swadener et al., 1999; Mello, 2006), copper/sapphire bi-crystals (Kysar, 2001), functionalized silicon surfaces (Liechti et al., 2013; Na et al., 2016), and silicon/epoxy interfaces (Gowrishankar et al., 2012). The main advantage of this technique is that it provides high resolution for suitably transparent adherends. However, the technique only provides normal crack opening displacements hence cannot be used to determine shear interactions.

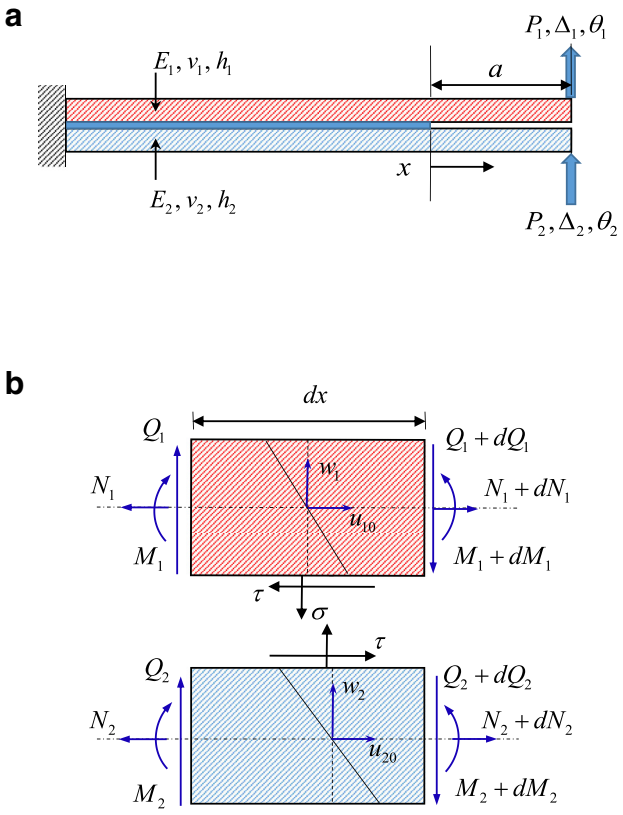

Fig. 1. (a) General specimen configuration, (b) free body diagrams of interacting beam elements.

In the present study, these considerations motivated the choice of asymmetric laminated beam specimens with two different end loading conditions with measurements of end loads, load point displacements and rotations to determine the normal and shear crack tip displacements. This allowed tensile and shear traction–separation relations to be measured simultaneously at each of the mode-mixes that were considered.

2. Analysis

The analysis presented here first establishes the theoretical basis for simultaneously extracting the normal and shear components of traction–separation relations for mixed-mode interactions between contacting surfaces in laminated beams. The next step is to evaluate the range of nominal mode-mix phase angles that could be obtained from the two end loading conditions (ELS and ENF).

2.1. Beam interaction analysis

An analysis of beam interactions based on simple beam theory is developed that accounts for the normal and shear interactions between the surfaces of two beams which have been brought into contact. The interactions could arise from chemical or physical connections between the surfaces. They could also include the presence of an interlayer, such as an adhesive; in that case, the relative displacements between the surfaces of the beams includes the bulk deformation of the interlayer as well as the two sets of interfacial displacements between the interlayer and the beams. No *a priori* assumptions are required as to the functional form of the interactions.

The laminated beam specimen formed by two interacting beams is clamped at one end and loaded at the other end (Fig. 1a). The upper and lower beams have, respectively, Young's moduli (E_1, E_2), Poisson's ratios (ν_1, ν_2), and heights (h_1, h_2). The initial crack length along the interface between the two beams is designated as a. The end-loads, end-displacements, and end-rotations are labeled as $(P_1, \Delta_1, \theta_1)$ and $(P_2, \Delta_2, \theta_2)$ for the upper and lower beams, respectively.

Considering an infinitesimal section of the specimen (Fig. 1b), the displacement fields in the upper and lower beams are approximately

$$u_1(x, z_1) = u_{10} - z_1 \frac{dw_1}{dx},\ w_1 = w_1(x, 0), \tag{1}$$

$$u_2(x, z_2) = u_{20} - z_2 \frac{dw_2}{dx},\ w_2 = w_2(x, 0), \tag{2}$$

where u_{i0} $(i = 1, 2)$ are the axial displacements at the neutral axis of each adherend, and w_i are the lateral deflections of each adherend. Here, following the classical Euler beam theory, we ignore the shear strain in the beams as well as Poisson's effect for the lateral displacement. As a result, the relative normal and tangential displacements between the bottom surface of the upper beam and the top surface of the lower beam are

$$\delta_n = w_1 - w_2 \text{ and } \delta_t = u_{1b} - u_{2t}, \tag{3}$$

respectively, with

$$u_{1b} = u_{10} + \frac{h_1}{2}\frac{dw_1}{dx}, \tag{4}$$

$$u_{2t} = u_{20} - \frac{h_2}{2}\frac{dw_2}{dx}. \tag{5}$$

Note that, in this analysis, if there is an adhesive layer between the adherends, δ_n, δ_t would include the deformation of the adhesive as well as those of the interfaces with the upper and lower beams. A scheme for subtracting out the deformation of any adhesive is discussed later.

Having established the kinematics in Eqs. (1–5), differential equations for the normal and tangential displacements across the interface can be derived (see details in Appendix A) from equilibrium equations for the two linearly elastic beams. The governing equation for the normal component is

$$\delta_n{}^{(4)} = -\left(\frac{1}{D_1} + \frac{1}{D_2}\right)\sigma - \left(\frac{h_1}{2D_1} - \frac{h_2}{2D_2}\right)\tau', \tag{6}$$

while for the tangential component it is

$$\delta_t'' + \left(\frac{P_1 h_1}{2D_1} + \frac{P_2 h_2}{2D_2}\right) + \left(\frac{h_2}{2D_2} - \frac{h_1}{2D_1}\right)\int_0^x \sigma\, dx = \left(\frac{1}{A_1} + \frac{1}{A_2} + \frac{h_1^2}{4D_1} + \frac{h_2^2}{4D_2}\right)\tau. \tag{7}$$

These two equations are clearly coupled in the sense that the relative normal and tangential displacements between the two interacting surfaces each depends on both the normal (σ) and shear (τ) components of the traction between the two surfaces. The quantities (A_i, D_i) are the axial and bending stiffness of each beam as defined in Appendix A. Interestingly, Eqs. (6–7) can be decoupled if $\frac{h_1}{D_1} = \frac{h_2}{D_2}$. When this "balance" condition applies, the governing equations simplify to

$$\delta_n{}^{(4)} = -\left(\frac{1}{D_1} + \frac{1}{D_2}\right)\sigma, \tag{8}$$

and

$$\delta_t'' + \left(\frac{P_1 h_1}{2D_1} + \frac{P_2 h_2}{2D_2}\right) = \left(\frac{1}{A_1} + \frac{1}{A_2} + \frac{h_1^2}{4D_1} + \frac{h_2^2}{4D_2}\right)\tau. \tag{9}$$

Under the balance condition, a simple beam analysis (Appendix A) was used to obtain the normal and tangential crack tip displacements in terms of the end loads, end displacements and rotations of each beam as

$$\delta_n^* = \Delta_1 - \Delta_2 - a(\theta_1 - \theta_2) + \frac{a^3}{6}\left(\frac{P_1}{D_1} - \frac{P_2}{D_2}\right), \tag{10}$$

and

$$\delta_t^* = \frac{1}{2}(h_1\theta_1 + h_2\theta_2) - \frac{P h_1 a^2}{4D_1}, \tag{11}$$

where $P = P_1 + P_2$.

Moreover, under the balance condition, the normal and shear components of the J-integral are also decoupled (Appendix A) and they can be obtained as

$$J_{\mathrm{I}} = \hat{D}\left(\frac{P_1}{D_1} - \frac{P_2}{D_2}\right)(\theta_1 - \theta_2), \tag{12}$$

and

$$J_{\mathrm{II}} = \frac{\hat{A} h_1}{4D_1} P(h_2\theta_2 + h_1\theta_1), \tag{13}$$

where $\hat{A} \equiv (\frac{1}{A_1} + \frac{1}{A_2} + \frac{h_1^2}{4D_1} + \frac{h_2^2}{4D_2})^{-1}$ and $\hat{D} \equiv (\frac{1}{D_1} + \frac{1}{D_2})^{-1}$. We note that the partition of the J-integral relies on the calculations of the crack-tip traction and separation in terms of the remote parameters (end force, displacement, and rotation) as given by Eqs. (A.20) and (A.22), which is made possible by the simple beam assumptions and the balance condition.

By definition, the components of the J-integral can be calculated with a contour along the interface ahead of the crack tip (i.e., $-\infty < x < 0$) surrounding the entire cohesive zone as

$$J_{\mathrm{I}} = \int_{-\infty}^{0} \sigma \left(\frac{d\delta_n}{dx} \right) dx = \int_{0}^{\delta_n^*} \sigma \, d\delta_n, \tag{14}$$

and

$$J_{\mathrm{II}} = \int_{-\infty}^{0} \tau \left(\frac{d\delta_t}{dx} \right) dx = \int_{0}^{\delta_t^*} \tau \, d\delta_t. \tag{15}$$

Then, the normal and shear traction–separation relations can be determined by taking the derivatives, $\sigma^* = \frac{dJ_{\mathrm{I}}}{d\delta_n^*}$ and $\tau^* = \frac{dJ_{\mathrm{II}}}{d\delta_t^*}$, using the respective values of the J-integrals and the crack tip displacements from Eqs. (10 to 13) based on measured end loads and end displacements and rotations of each adherend. The total J-integral as the energy release rate for crack growth is then, $J = J_I + J_{II}$, under the mixed-mode condition. We note that the tractions in general cannot be determined by the derivatives of the total J-integral with respect to the corresponding crack-tip displacements due to coupling of the traction–separation relations in the normal and shear directions under a mixed mode condition (Wu et al., 2016). It is the partition of the total J-integral into the two components as in Eqs. (12–13) that allows the traction components be determined simultaneously by the derivatives.

To implement the proposed method, a custom loading device (Fig. 2a) was developed to conduct experiments using the end-loaded split (ELS) and end-notched flexure (ENF) configurations (Fig. 2b). In the ELS experiments, only the top adherend is loaded, which means that $P_2 = 0$ and $P = P_1$ was measured by the load cell as shown in Fig. 2c. In the ENF experiments, $\Delta_1 = \Delta_2$, and the total force P was measured. However, the calculation of the mode-I J-integral (Eq. 12) requires the individual end forces (P_1, P_2). While independent measurements of both could be made by adding a strain measurement on the lower adherend, there was insufficient room to apply a strain gage to the specimen and strain gaging every specimen is costly. On the other hand, it is relatively straightforward to measure the normal crack opening displacement (NCOD) using the infrared crack opening interferometry (IR-COI) technique (Liechti, 1993; Gowrishankar et al., 2012). With the measurement of NCOD at the crack tip (δ_n^*), the end load on the top adherend of the ENF specimen can be obtained from (Eq. 10) as,

$$P_1 = \hat{D} \left\{ \frac{P}{D_2} + \frac{6}{a^3} [\delta_n^* + (\theta_1 - \theta_2) a] \right\}, \tag{16}$$

and Eq. (12) becomes

$$J_{\mathrm{I}} = \frac{6\hat{D}}{a^2} \left[(\theta_1 - \theta_2)^2 + \frac{\delta_n^*}{a} (\theta_1 - \theta_2) \right]. \tag{17}$$

2.2. Nominal mode-mix

The ELS and ENF configurations, with equal adherends, only provide two mode-mix conditions. As indicated in the introduction, the range of mode-mix can be greatly expanded by considering asymmetric configurations of each specimen while maintaining the balance condition that decouples the differential equations for the normal and shear interactions between the adherends. In particular, by using different materials for the bottom adherend of the sandwich specimens (Fig. 2b), we obtained nominal phase angles of mode-mix ranging from $-53°$ to $87.5°$ (Fig. 3) for a silicon/epoxy interface in the present study.

The determination of mode-mix in laminated beam specimens has suffered from some ambiguity in the literature in the sense that different methods (Hutchinson and Suo, 1992; Williams et al., 1988) provide, in some situations, widely differing values. At one end of the spectrum of the approaches (Hutchinson and Suo, 1992), the definition of mode-mix is based on the singular stress field around the crack front when linearly elastic fracture mechanics is applied. The other extreme arises when the stress state is obtained from simple beam kinematics (Williams et al., 1988). While the former is strictly applicable to the cases of small-scale bridging, the latter may be a good approximation for large-scale bridging (Charalambides et al., 1992). Davidson et al., (1997) explored an alternative approach for determining mode-mix in delaminating composites. The differences in all the approaches are currently being reconciled (Conroy et al., 2015). Preliminary results indicate that this ambiguity does not arise when the beams satisfy the balance condition (Wu, 2016).

Nevertheless, the approach that was taken here follows Hutchinson and Suo (1992), with the viewpoint that the phase angles of mode-mix are extracted as the nominal or global mode-mixes to form a point of reference for discussion. Furthermore, because the applied end loads and displacements are following proportional paths, the nominal mode-mix is fixed in each ELS or ENF experiment. The data obtained from the experiments indicate that the local tractions and displacements that develop in the cohesive zone are generally not proportional and the local mode-mix becomes complicated as damage initiates and progresses (Sills and Thouless, 2013). Thus in general, the nominal mode-mix does not predict the partition of fracture energy at the crack tip.

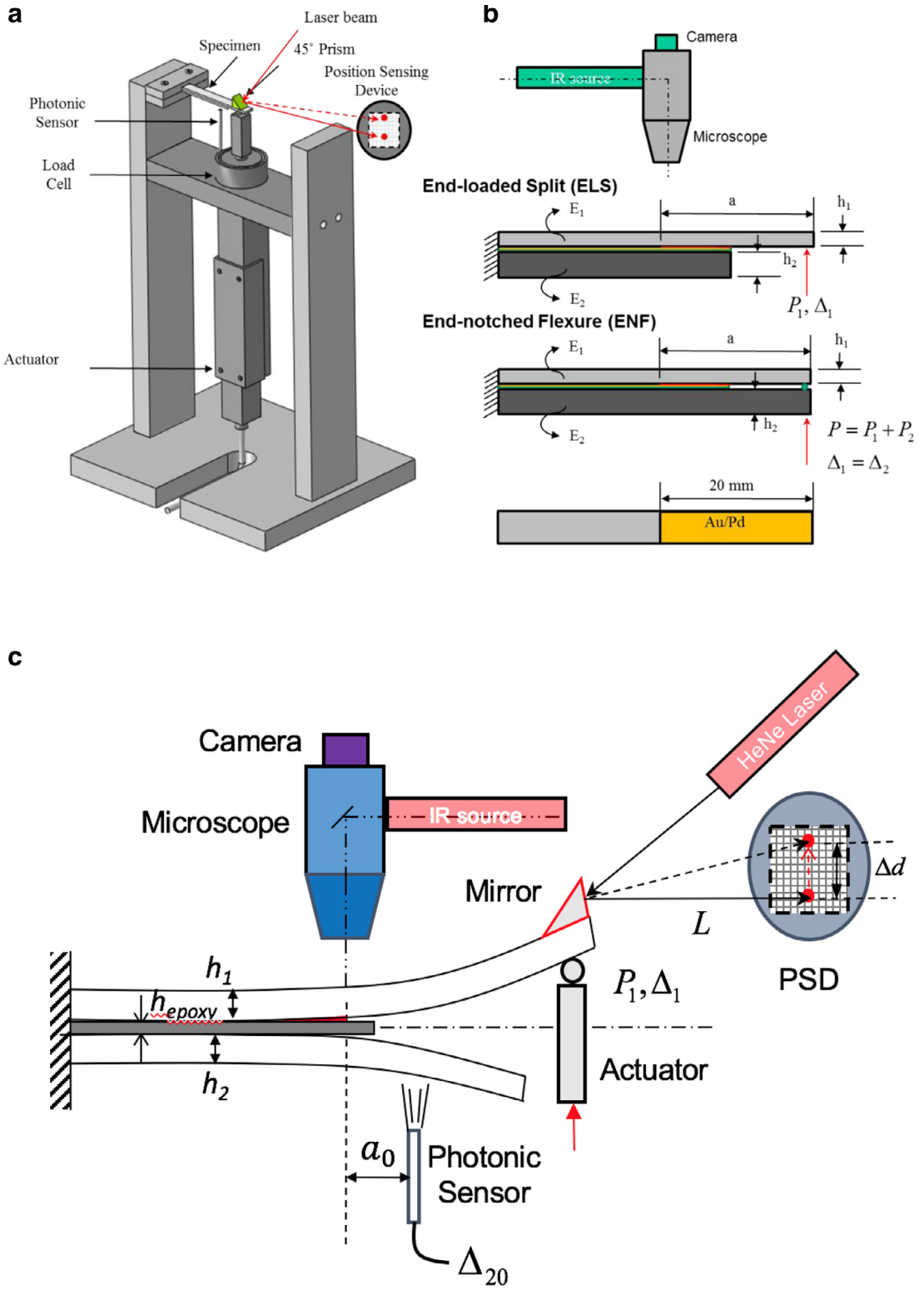

Fig. 2. (a) Schematic of the loading device, (b) specimen configurations, and (c) side view of the apparatus.

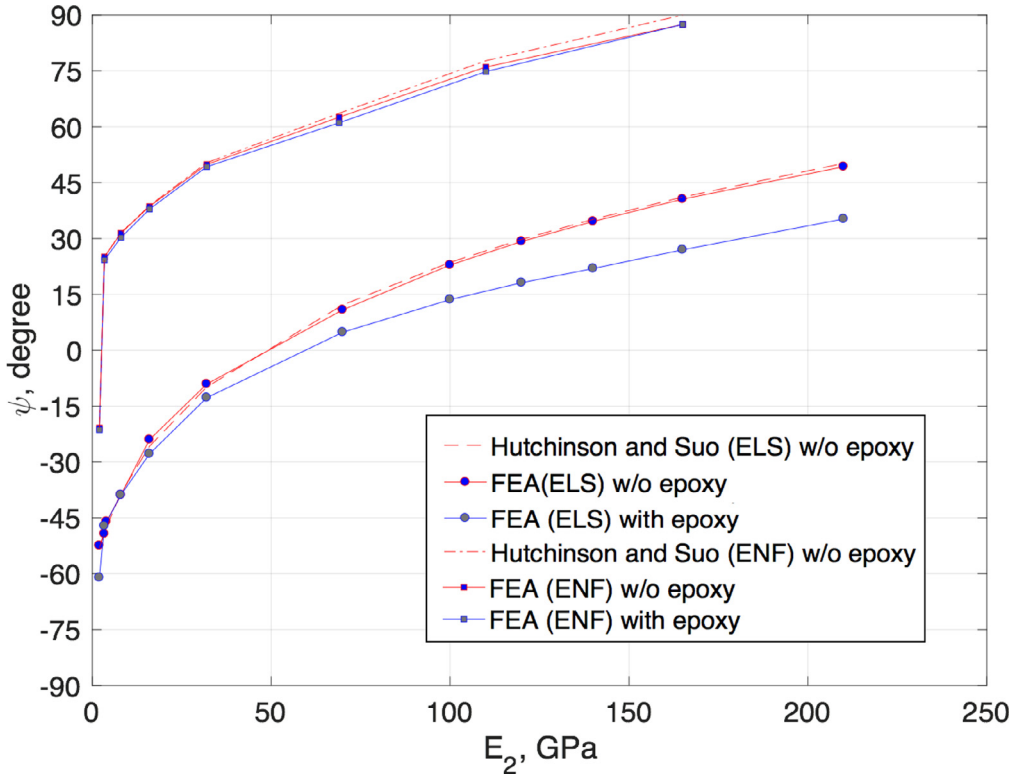

Fig. 3. Nominal mode-mix phase angles obtained by varying Young's modulus of the bottom adherend and its thickness simultaneously under the balance condition, with a silicon top adherend.

The semi-analytical approach (Hutchinson and Suo, 1992) recognizes the ELS and ENF specimens as bilayer structures where the complex stress intensity factor can be written as

$$K = {h_1}^{-i\varepsilon}\left(\frac{1-\alpha}{1-\beta^2}\right)^{1/2}\left(-\frac{C_2M_3}{\sqrt{2h_1^3U}} - ie^{i\gamma}\frac{M_1 - C_3M_3}{\sqrt{2h_1^3V}}\right)e^{i\omega}, \tag{18}$$

where the detailed definition of the parameters is provided in Appendix B for completeness.

For a range of values of E_2 and ν_2, the Young's modulus and Poisson's ratio of the bottom beam, with corresponding values of h_2 required to maintain the balance condition established by the desire to maintain an upper adherend made of silicon ($E_1 = 165$GPa and $\nu_1 = 0.28$) with a thickness of 1.0 mm (h_1) for all the experiments conducted in this study, the nominal mode-mix phase angles for the ELS and ENF configurations are obtained based on the complex stress intensity factors in Eq. (18) as

$$\psi = \tan^{-1}\left(\frac{\mathrm{Im}\left(Kl^{i\varepsilon}\right)}{\mathrm{Re}\left(Kl^{i\varepsilon}\right)}\right), \tag{19}$$

where l is taken to be 50 μm, equal to the thickness of the epoxy layer employed in the experiments.

The semi-analytical solution in Eq. (18) essentially assumes the adhesive layer to be infinitesimally thin between the two beams. The mode-mix phase angles obtained in this way are compared with those obtained using a finite element model (Wu, 2016) that initially ignored the presence of the epoxy layer for purpose of comparison. The two sets of results are in close agreement (Fig. 3). A second set of finite element analyses was then conducted, considering an epoxy thickness of 50 μm, the nominal value employed in all experiments. In this model, the crack is assumed to grow along the interface between the upper beam (Si) and the epoxy, while the Young's modulus and thickness of the lower beam are varied simultaneously according to the balance condition. Similar finite element analyses were conducted in Wu et al. (2016), where the epoxy thickness was varied in the ELS specimens to obtain different phase angles over a relatively small range. It can be seen (Fig. 3) that the epoxy layer causes a slight shift in the phase angle for the ELS specimens, especially for the cases with a lower beam that has a relatively high Young's modulus. However, it does not have much effect on the ENF specimens. The nominal mode-mix phase angles that were used in this study are summarized in Table 1 along with details of the properties and thickness of the bottom adherend that were used. The epoxy thickness was well controlled with an average deviation

Table 1
Specimen details and mode-mix.

Configuration	Materials for bottom adherend	Poisson's ratio	Young's modulus E_2 (GPa)	Thickness h_2 (mm)	ψ (°) with epoxy
ELS	Acrylic	0.3	3.4	6.97	−53.1
ELS	Glassy polymer	0.28	8	4.54	−39.8
ELS	Glass-filled polymer	0.29	16	3.21	−27.8
ELS	Aluminum	0.3	70	1.54	4.8
ELS	Copper	0.3	120	1.17	18.1
ELS	Silicon	0.28	165	1.00	27.0
ELS	Stainless steel	0.27	210	0.89	35.3
ENF	Aluminum	0.3	69	1.55	61.1
ENF	Copper	0.3	110	1.22	74.8
ENF	Silicon	0.28	165	1.00	87.5

of ± 5 μm that resulted in a deviation in the phase angle of approximately ± 1.5°. By making use of both ELS and ENF specimens, the nominal mode-mix obtained in this study spanned a wide range of phase angles from −53° to 87.5°. For the ELS specimen, it can be observed that the thickness of the bottom adherend increased as the Young's modulus E_2 decreased. For the case of an acrylic bottom adherend, the required thickness, which is the largest of all bottom adherends considered, is slightly more than 1/10 of the initial crack length, reaching the upper limit for applicability of the simple beam theory. At the opposite extreme, when E_2 exceeded 210 GPa (stainless steel), it became challenging to produce adherends with a thickness below 1 mm. This was the main reason why the ENF configuration was selected to extend the mode-mix range to the upper end of shear dominance (mode II).

3. Experiment

In this section, we describe the preparation of the specimens and the manner in which the experiments were conducted.

3.1. Specimen preparation

All the specimens consisted of two beams joined by a layer of epoxy. All of the top beams and some of the bottom ones were cut from n-type Si (111) wafers supplied by WRS Materials. The wafers were 50 mm in diameter and nominally 1 mm thick. They were polished on both sides to facilitate the use of IR-COI. An automatic dicer (Disco, model DAD 321) was used for cutting wafers into 50 by 5 mm strips for the top adherend and the strips were then cleaned individually by ultra-sonication in de-ionized water to remove any debris accumulated during dicing. To maintain the balance condition while achieving different mode-mix phase angles, the bottom adherends were made out of different materials as listed in Table 1. For all specimens, the top adherend was coated with an Au/Pd thin film from one end of the strip to a length of about 19.5 mm. The relatively low adhesion energy between Au/Pd coating and epoxy ($\sim$0.07 J/m^2) allowed an initial crack to form with minimal damage before fracture of the silicon/epoxy interface. A two-component epoxy system (EP30, Masterbond®) was used as the adhesive layer. The epoxy mixture was de-gassed in a vacuum chamber upon mixing. The specimens were then cured at room temperature for 72 h.

Two different lengths were prepared for the bottom adherends of the two experimental configurations (Fig. 2b): 40 mm for ELS and 50 mm for ENF. It should be noted here that, for the ENF specimen, a thin metal wire (copper) was used between the top and bottom adherends in order to reduce the potential effect of friction (Carlson et al., 2011) between the fracture surfaces of the upper and lower adherends.

3.2. Measurements

Schematics of the apparatus and the specimen geometry are shown in Fig. 2. The loading device is a slightly modified version of the one that was used previously (Wu et al., 2016). In the ELS experiments, the end-displacement of the upper beam was controlled at a rate of 1 μm/s based on the displacement sensor of the actuator. The same rate was applied for the ENF experiments, where the end-displacement was the same for the upper and lower beams.

In addition to the end load, the end displacements and rotations of each beam were measured in the present study. In the ELS experiment (Fig. 2c), the end rotation of the top adherend was measured by mounting a 45° mirror on the free surface of the upper adherend right above the loading point. The mirror reflected an incident laser beam onto a position sensing detector (PSD, Thorlabs, PDP90A). Given the distance L between the detector and the mirror, the end-rotation of the silicon beam is related to the vertical movement (Δd) in the detector as: $\theta_1 = \frac{1}{2}\arctan(\Delta d/L)$. The resolution of the end-rotation measurement is then estimated to be at $\sim 10^{-4}$ rad for $L = 10$ mm and the PSD resolution at 1 μm. In order to determine the end rotation of the lower adherend, a photonic sensor (MTI, KD-245) with a resolution of 100 nm was placed at a distance a_0 behind the initial crack front to measure the deflection Δ_{20} of the lower adherend, with which the end-rotation of the lower adherend was obtained approximately as $\theta_2 \approx \Delta_{20}/a_0$. This approximation is justified because the lower adherend of the ELS specimen undergoes a rigid-body rotation from the initial crack front to the free end and the

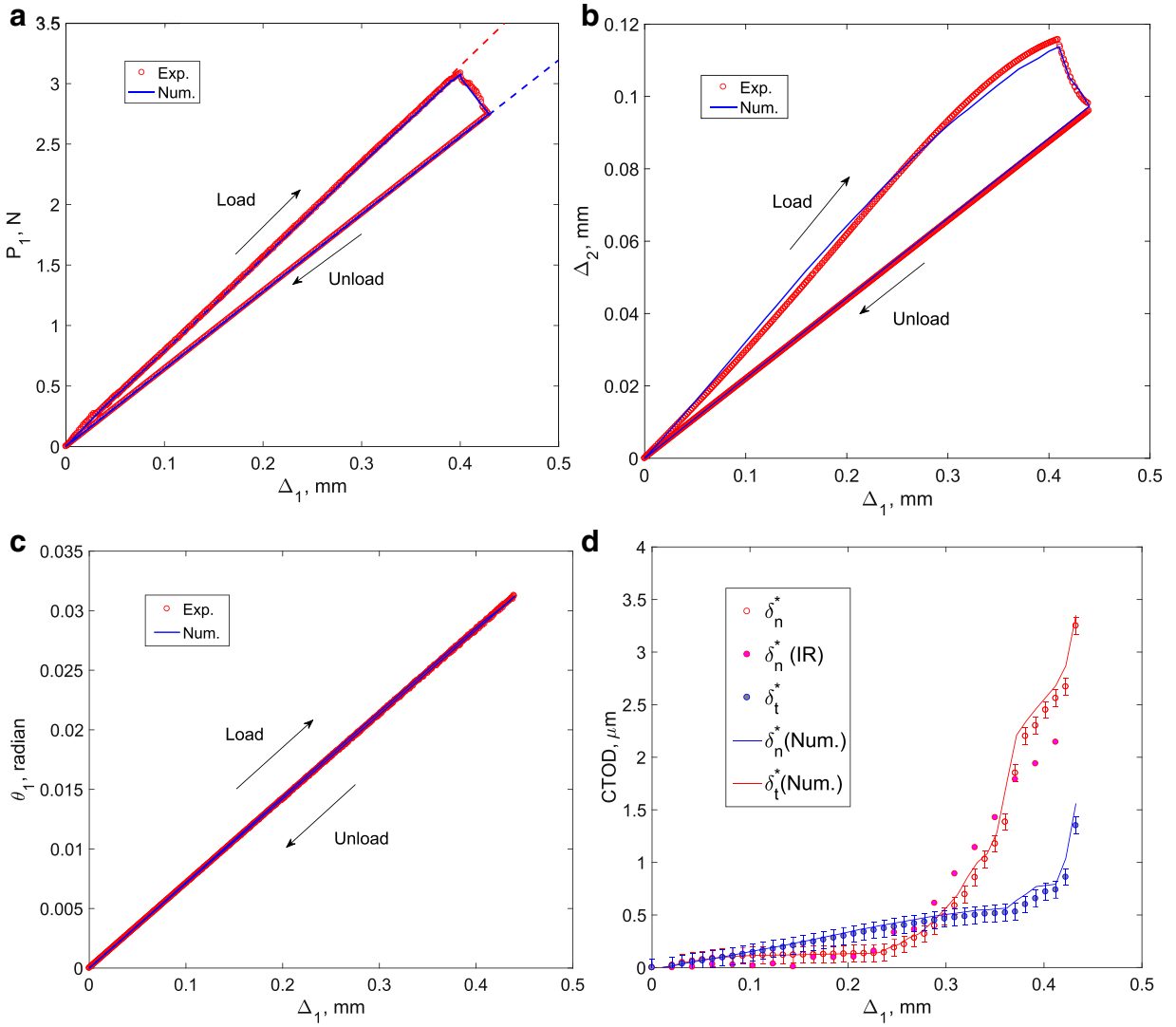

Fig. 4. Responses of an ELS specimen with silicon as the bottom adherend ($\psi = 27^\circ$): (a) force–displacement response, (b) end-displacements, (c) end-rotation, and (d) normal and shear crack-tip displacements.

deflection of the lower adherend at the location of the initial crack front was found to be negligible both experimentally and numerically (see additional information in Supplementary Material). Similarly, the end displacement of the lower adherend was obtained approximately by linear extrapolation as $\Delta_2 = (a/a_0)\Delta_{20}$. The corresponding resolution for the crack-tip displacements obtained from Eqs. (10) and (11) was about 100 nm. Error bars in these deduced crack-tip displacements are shown to reflect this resolution (Fig. 4d).

For the ENF specimen, the end-rotation of the upper beam was measured in the same way as for the ELS specimen. In order to determine the end rotation of the lower adherend, a photonic sensor (MTI, KD-245) was again used to measure the deflection Δ_{20} of the lower beam at a distance a_0 behind the initial crack front, with which the end-rotation of the lower adherend was obtained approximately as $\theta_2 \approx (\Delta_2 - \Delta_{20})/(a - a_0)$. This approximation is justified by placing the photonic sensor close to the loading point so that $a - a_0$ is small.[a] As noted earlier, the normal crack-tip displacement of the ENF specimen was measured by using the IR-COI technique, which has a resolution of 20 nm. On the other hand, the resolution for the tangential crack-tip displacement obtained from Eq. (11) was about 100 nm.

Classical crack opening interferometry was used to measure the normal crack opening displacement (NCOD) and crack length as silicon is transparent to infra-red. The measured NCOD served as a validation of the extracted NCOD for the ELS

[a] Strictly, for the ENF specimen, the end rotation of the lower adherend can be determined as: $\theta_2 = (\Delta_2 - \Delta_{20})/(a - a_0) - P_2(a - a_0)^2/(6D_2)$, where the second term on the right-hand side is relatively small compared to the first term if $a - a_0$ is small. Supporting information can be found in the supplementary materials.

specimens. In the ENF experiments, the NCOD measurements were used to calculate the applied force for each beam at far end of the specimens. This infrared crack opening interferometry (IR-COI) technique (Gowrishankar et al., 2012) essentially uses the interference between the two rays reflected from the crack surfaces to determine the distance between them. The normal infra-red incident beam (Fig. 2c) was provided using an infrared microscope (Olympus BH2-UMA) that was fitted with an internal beam splitter and an IR filter (1040 ± 15 nm). The images of the region near the crack front were obtained using a digital camera (Lumenera Corporation, Infinity 3) with a resolution of 1392×1040 pixels. The images were then processed to determine the NCOD with a resolution of 20 nm. It should be noted here that, in this experiment, all data were collected and synchronized within single Labview® control program.

4. Results

This section begins with a presentation of the basic data that was obtained from a symmetric ELS specimen with a nominal mode-mix phase angle of 27°. The basic data is then transformed into derived quantities of interest (J-integral, crack tip displacements and traction–separation relations). The results of the experiments that were conducted at all the other mode-mixes are then summarized and form the basis of further discussion.

4.1. CTOD, J-integral, and TSRs

The force versus applied end displacement response for an ELS specimen with silicon as the bottom adherend is shown in Fig. 4a. The response was initially linear and started to exhibit slightly nonlinear behavior after an applied displacement of approximately 0.2 mm, as emphasized by the deviation from the dashed straight line. When the force was about to reach its maximum, this nonlinear behavior became more significant. This portion of the nonlinear behavior is related to the development of the cohesive zone ahead of the initial crack tip. The force then decreased from its peak value, indicating that the cohesive zone had fully developed and steady-state crack growth ensued. A linear response was found for a subsequent unloading, which had a lower stiffness, thereby confirming that crack extension had indeed occurred during the loading segment. The corresponding variation in end-displacement (Δ_2) of the bottom adherend is shown in Fig. 4b. The response was again initially linear followed by a nonlinearly increasing portion as the cohesive zone developed and then a decreasing portion during steady-state crack growth. Again, the response was linear for subsequent unloading. The end-rotation of the top adherend responded linearly during both the loading and unloading processes (Fig. 4c).

The normal and shear components of the CTOD were obtained using Eqs. (10–11) and are plotted (Fig. 4d) versus the applied displacement. The error bars were obtained through an uncertainty analysis based on the resolutions of the position sensing device and photonic sensor. The normal CTOD measured using IR-COI are also plotted for comparison/validation purposes. It is observed that normal CTOD determined from global parameters and beam theory had a similar response to those measured locally by IR-COI. Close agreement was observed from both the linear stage, the concurrent turning point ($\Delta_1 \sim 0.2$ mm), and the nonlinear stage. Especially in the linear stage, most of the IR-COI data fell within the error bar range of the deduced normal CTOD results. This close agreement demonstrated the validity of the proposed method for obtaining normal CTOD from far-field measurements. The normal CTOD reached 2.5 μm as the force reached its peak ($\Delta_1 = 0.4$ mm). The corresponding shear CTOD was much lower at the peak force. However, the shear CTOD was at the same level and even higher than the normal CTOD in the earlier stage. This indicated that a non-proportional CTOD path was followed in the cohesive zone in spite of the nearly proportional end displacements as applied up to the point of steady-state crack growth (Fig. 4b), suggesting that the damage processes for normal and shear interactions might have initiated at different points in time.

The calculated J-integrals for both normal and shear interactions using Eqs. (12–13) are plotted against the applied end-displacement and associated CTOD in Fig. 5a and b. In the early stage of loading ($\Delta_1 < 0.1$ mm), while the increments in CTOD were small (Fig. 4d), the corresponding J-integral values also increased slowly. The normal interactions reached an elastic limit of around $1\,\mathrm{J/m^2}$ at $\Delta_1 \sim 0.2$ mm, after which both the normal CTOD and J_1 increased more rapidly. The shear interaction reached its elastic limit of $\sim 9\,\mathrm{J/m^2}$ much later at $\Delta_1 \sim 0.35$ mm. The elastic limits are evident as the inflection points when plotting the J-integrals versus CTODs in Fig. 5b. Both components of the J-integral reached their steady-state values of 7.5 and $10\,\mathrm{J/m^2}$ simultaneously at $\Delta_1 \sim 0.4$ mm. The normal and shear components of the interfacial toughness are then obtained from the steady-state values of the J-integral components as Γ_n and Γ_t, and the total toughness is $\Gamma = \Gamma_n + \Gamma_t$. It is interesting to observe that Γ_t was greater than Γ_n by almost 25% at the nominal phase angle of 27° under consideration. As noted earlier, the nominal phase angle does not predict the partition of fracture energy. It should also be noted here that the estimated error in calculating the J-integrals was so small that the error bars are smaller than the symbols shown in the figure.

Upon taking the numerical derivatives of the J-integrals with respect to their respective CTOD, the resulting traction–separation relations (TSRs) in both directions are obtained in Fig. 6. In the normal traction–separation relation, an initially stiffening response was observed. In the past, the response prior to the maximum traction has been commonly represented by linearly elastic behavior (e.g., Sills and Thouless, 2013; Wu et al., 2016). While time constraints have not allowed further investigation to determine if the observed stiffening behavior was elastic, a stiffening response is certainly consistent with rubber-like behavior and may relate to randomly oriented polymer chains in the epoxy interphase being increasingly aligned normal to the interface as the loading is increased. The normal traction reached its peak at a normal separation of

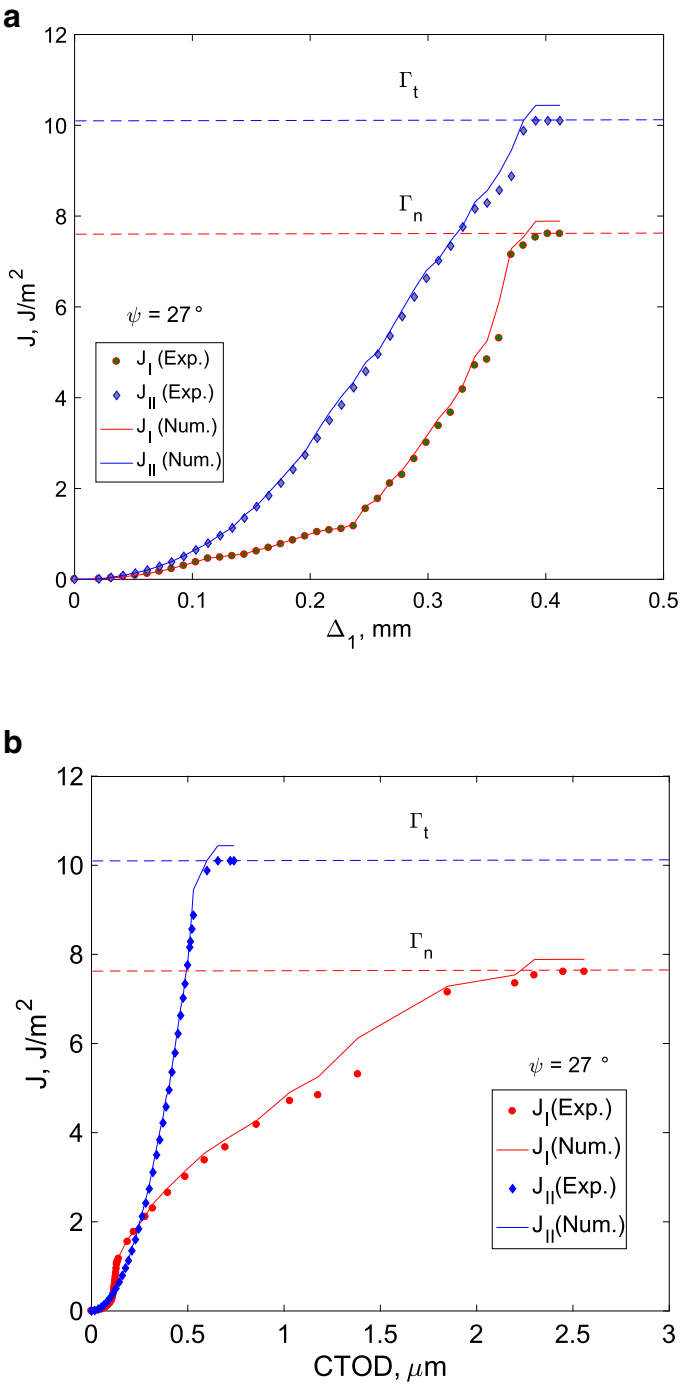

Fig. 5. Derived J-integrals for an ELS specimen with $\psi = 27^{\circ}$. (a) J-integrals versus applied end displacement, and (b) J-integrals versus corresponding CTOD.

approximately 0.13 μm which was larger than the values found in a previous work (Gowrishankar et al., 2012), albeit with a different epoxy. The peak strength was about 48 MPa, which was at the elastic limit of the epoxy (Na et al., 2015) used in the present study. After the peak, the normal traction dropped abruptly and eased into a plateau with an average value of about 2 MPa that ended at a normal separation of ~2.5 μm. The descending traction followed a power-law type function of separation, with a steeper decay than has been previously described by exponential functions (Gowrishankar et al., 2012; Wu et al., 2016; Cao et al., 2016; Na et al., 2015). The shear traction–separation relations had an essentially linear response till the shear traction reached its peak (~38 MPa) at a tangential separation of ~0.54 μm. After the peak, the shear traction

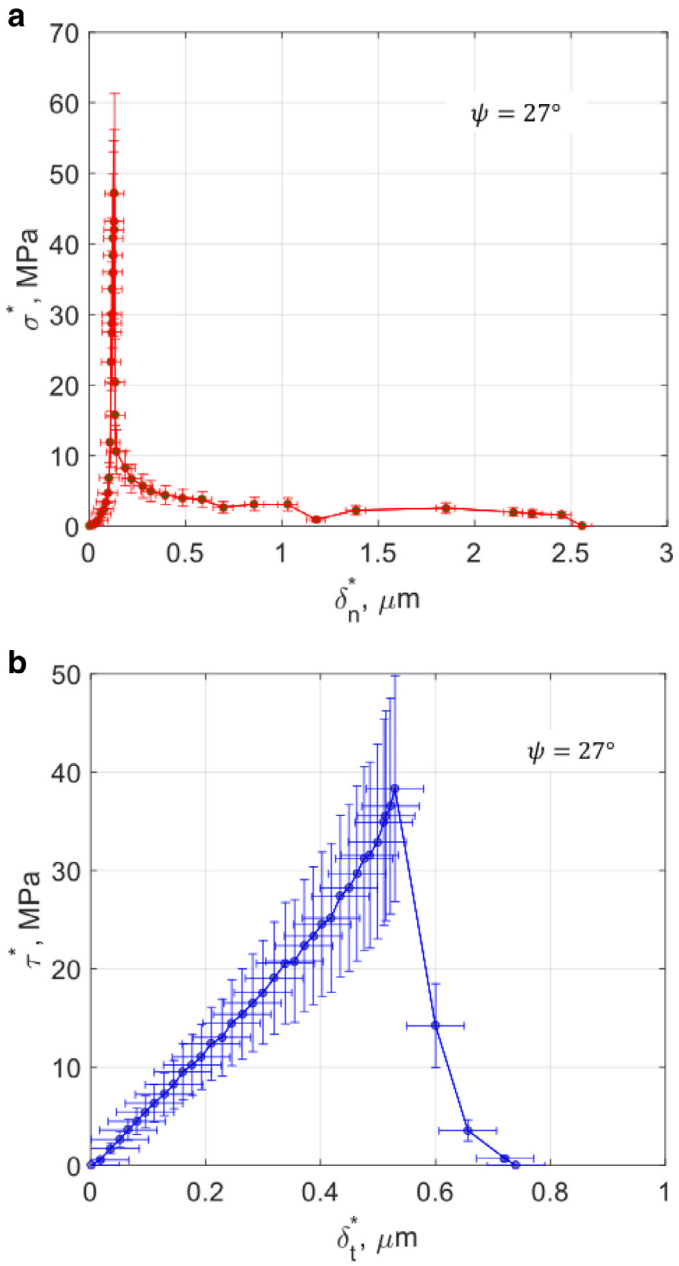

Fig. 6. (a) Normal and (b) shear traction–separation relations for an ELS specimen ($\psi = 27°$).

dropped very rapidly to zero for a total shear interaction range of about 0.7 μm, much smaller than the range of the tensile interaction.

Considering the dissimilarities in the normal and shear traction–separation relations, the development of the separations and tractions was examined in more detail (Fig. 7). The normal and shear crack-tip displacements are compared in Fig. 7a where a short linear segment terminates at point ①. After that, the normal CTOD remains nearly constant but the shear CTOD continues increasing. This stage ends at point ②, followed by more rapid growth in the normal CTOD while the shear CTOD increases slightly. After point ③, both components of the CTOD grow rapidly. The path taken in the J-integral space (Fig. 7b) also consists of four distinguishable segments. Initially there is parity in the growth of the J-integral components, followed by mode II dominance, then mode I dominance and ending with a jump in the mode II component. Apparently, despite the globally proportional loading, the ratio J_{II}/J_I is not a constant along the path and is not predicted by the nominal mode-mix as defined in Eq. (19). The corresponding critical points were labeled in a plot of the two crack-tip tractions versus applied end-displacement (Fig. 7c). Between zero and point ①, the response is almost linear for both tractions near

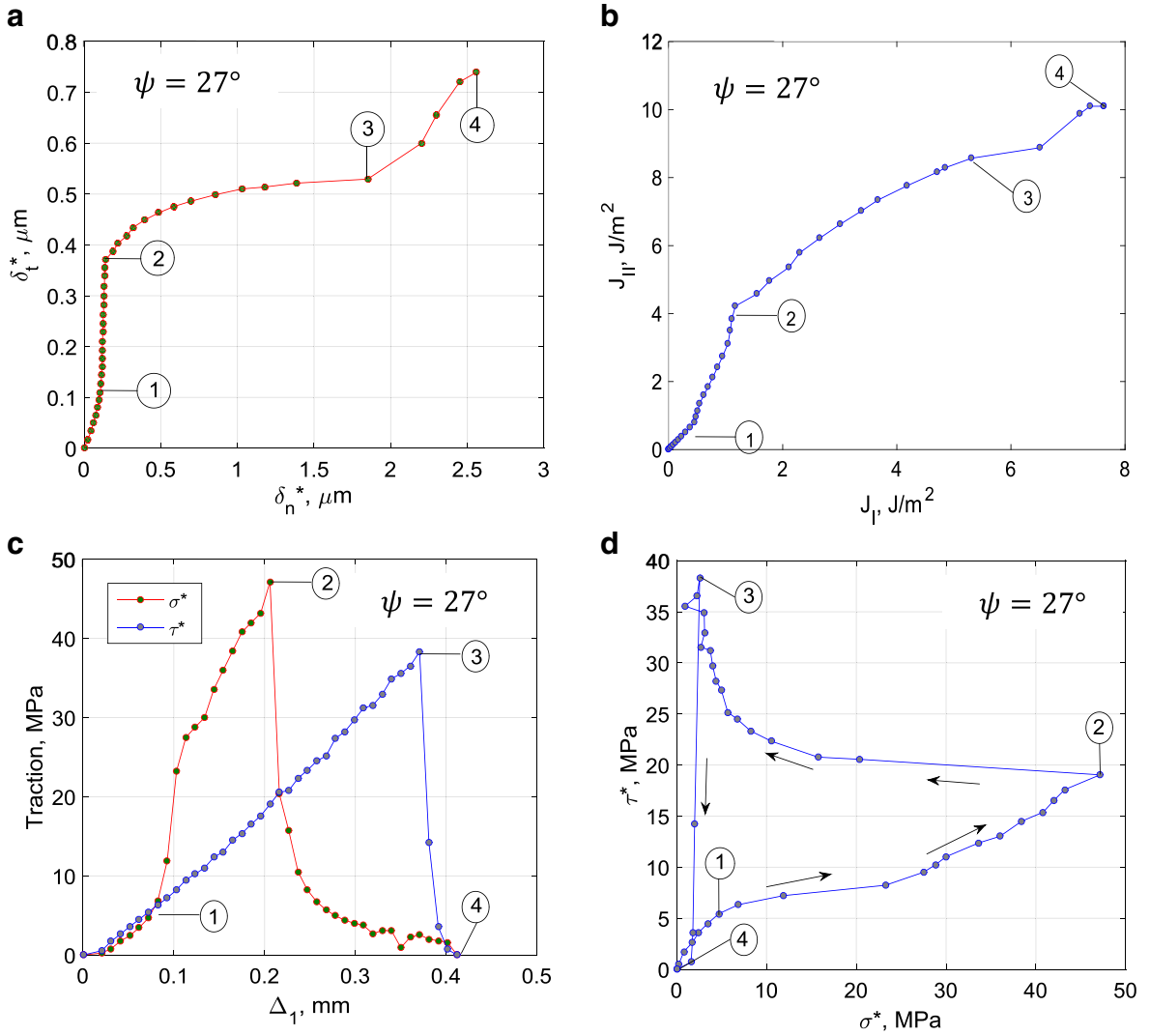

Fig. 7. Development of (a) normal and shear components of crack tip displacements, (b) components of the J-integral, (c) normal and shear tractions at the crack tip, and (d) the path taken by the crack tip tractions ($\psi = 27^{\circ}$).

the original crack front. After point ①, the normal traction increases much more rapidly than the linearly increasing shear traction. Thereafter ②, the normal traction decreases sharply while the shear traction continues increasing linearly. However, following point ③, the shear traction rapidly decays to zero simultaneously with the normal traction. Finally (Fig. 7d), it can be seen that path followed by the normal and shear tractions at the initial crack tip is by no means proportional. Clearly, the two tractions reached their peaks at two different loading points, with the maximum normal traction at ② and the maximum shear traction at ③. Therefore, the damage to the normal interaction started at ②, while the shear interaction remains undamaged until ③. This is in sharp contrast with most damage-based cohesive zone models where a single damage parameter is used for both the normal and shear interactions. Therefore, the damage processes in the normal and shear interactions are not coupled in the manner assumed by using a single damage parameter.

4.2. Mixed-mode effects

The variation in normal and shear traction–separation relations with mode-mix is now considered with a view to generalizing the results and examining some common representations of the mixed-mode interactions.

First, the mode-mix dependence of the toughness as well as its normal and shear components obtained from the steady-state J-integrals is shown in Fig. 8. The total toughness ($\Gamma = \Gamma_n + \Gamma_t$) and the shear component (Γ_t) both increased with increasingly positive and negative mode-mix phase angles, exhibiting similar asymmetric behavior with respect to mode-mix as noted previously for the toughness of glass/epoxy and sapphire/epoxy interfaces (Chai and Liechti, 1992; Liang and

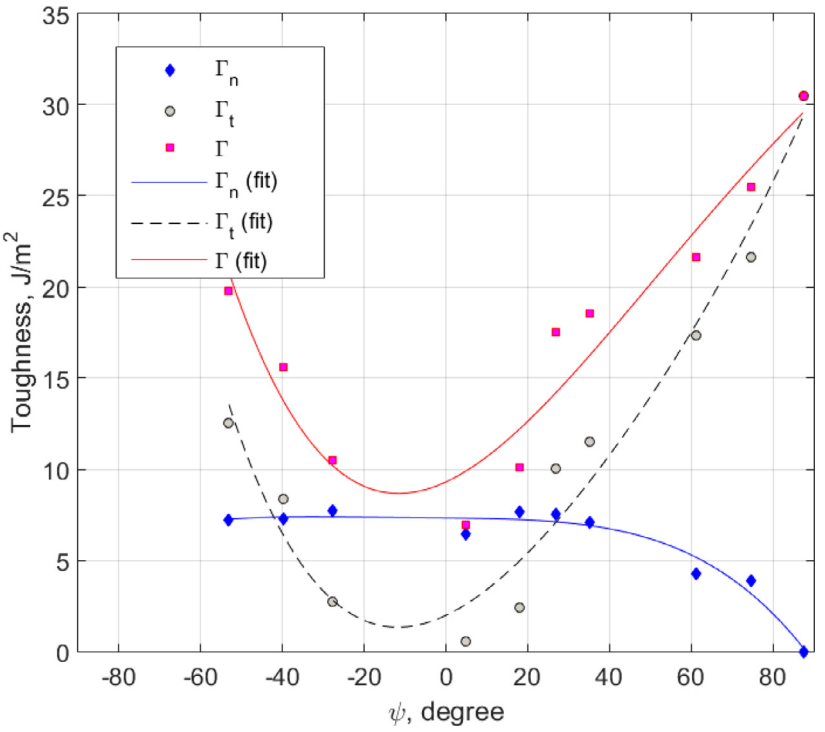

Fig. 8. Interfacial toughness versus phase angle of mode mix. The lines are polynomial fitting of the data.

Liechti, 1995; Swadener and Liechti, 1998; Mello and Liechti, 2006). The normal component (Γ_n) was essentially constant over a wide range of phase angles from −53° to 40° and then dropped to zero for phase angles close to 90°. This is consistent with the previous observations in Chai and Liechti (1992), Liang and Liechti (1995), Swadener and Liechti (1998), although it was not possible to examine phase angles greater than 60° in the previous works due to crack branching effects.

The normal component of the traction–separation relations extracted for lower mode-mix phase angles ($-53^\circ < \psi < 30^\circ$) are plotted in Fig. 9a while results for higher values ($30^\circ < \psi < 90^\circ$) appear in Fig. 9b. In preparation for generalizing the normal traction–separation relations as a function of mode-mix, each of the extracted traction–separation relations was fit to power laws of the form

$$\sigma(\delta_n) = \begin{cases} \sigma_0 \left(\frac{\delta_n}{\delta_{n0}}\right)^{\alpha}, & 0 < \delta_n < \delta_{n0} \\ \sigma_0 \left(\frac{\delta_{nc}-\delta_n}{\delta_{nc}-\delta_{n0}}\right)^{\beta_n}, & \delta_{n0} < \delta_n < \delta_{nc} \end{cases}, \tag{20}$$

where σ_0 is the normal strength, corresponding to the peak traction at the separation δ_{n0}, α and β_n are the power law exponents for the ascending and descending portions of the traction–separation relation. The range of normal interaction is defined by the critical normal separation, δ_{nc}, beyond which the normal traction is set be zero. For each TSR, σ_0 and δ_{n0} are determined first, and the exponent α for the ascending part is then obtained by fitting. For the descending part, the two additional parameters, δ_{nc} and β_n, are determined by fitting both the TSR and the normal component of toughness (Fig. 8). Following Eqs. (14) and (20), the normal component of toughness is obtained as

$$\Gamma_n = \int_0^{\delta_{nc}} \sigma(\delta_n) d\delta_n = \sigma_0 \left[\frac{\delta_{n0}}{1+\alpha} + \frac{\delta_{nc}-\delta_{n0}}{1+\beta_n} \right]. \tag{21}$$

The implication of Eq. (21) is that δ_{nc} can be determined for each β_n if the other parameters (σ_0, δ_{n0}, α, and Γ_n) are known.

The fitting parameters for the normal traction–separation relations are plotted as a function of the mode-mix phase angle (Fig. 10) and the actual values are given in Table 2. The three parameters, σ_0, δ_{n0} and α, were all essentially independent of mode-mix. This observation suggested that the ascending part of the normal TSR is independent of mode-mix, for which the three parameters could be averaged over all mode-mix and used thereafter. Following this idea, the average normal strength was found to be 42.63 MPa, δ_{n0} was 120 nm, and α was 4.5. The other two parameters, δ_{nc} and β_n, depend on mode-mix (Fig. 10c, d), where it can be seen that the largest normal interaction range was 2.7 μm followed by a noticeable decrease for mode-mix angles greater than 30°. It is near this mode-mix that shear interaction begins to dominate to such an extent that full slip has occurred before the normal tractions can fully develop. Interaction ranges at the micron level are clearly longer ranging than van der Waals or molecular interactions and are more likely associated with molecular pull out and/or

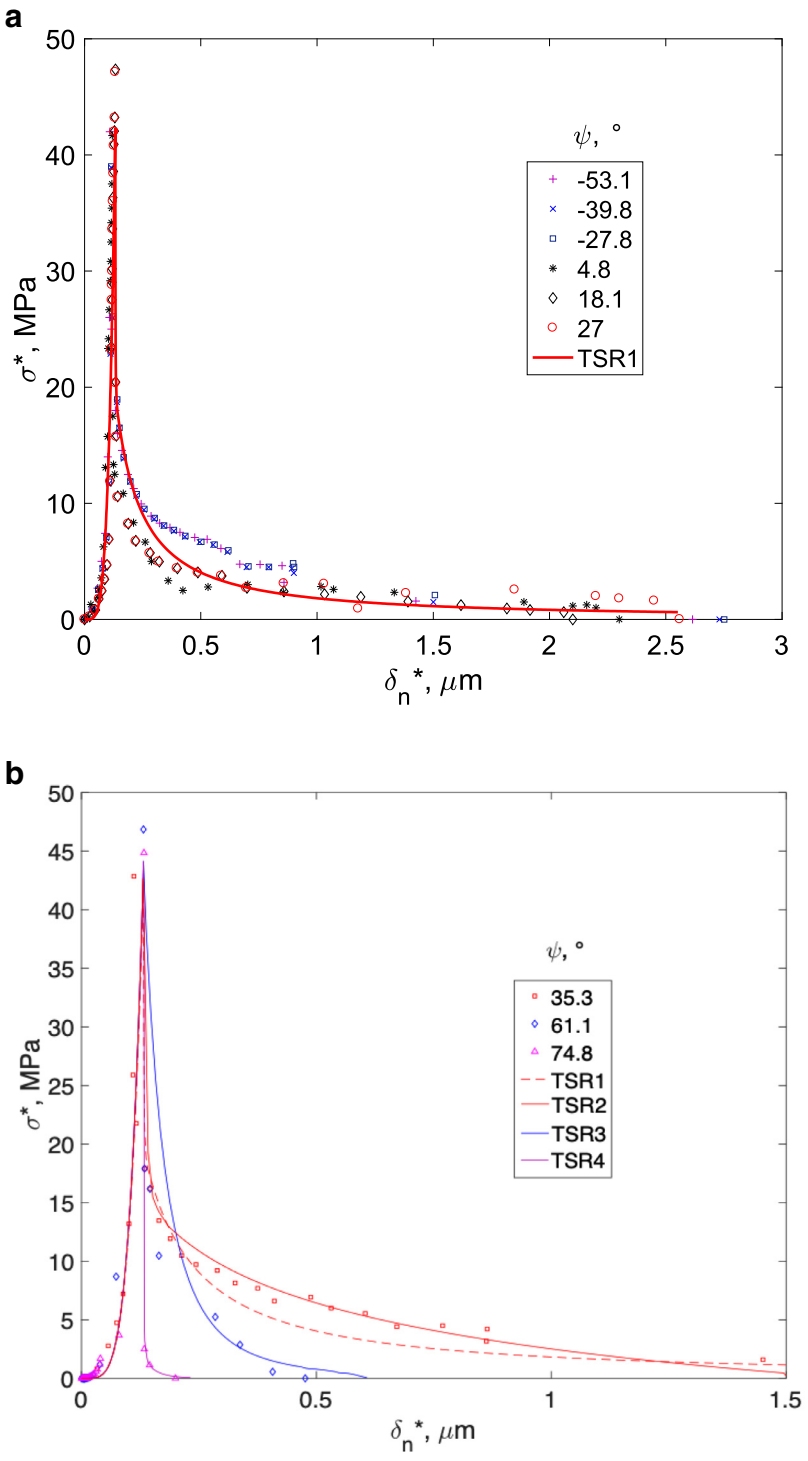

Fig. 9. Normal traction–separation relations for (a) low and (b) high mode-mix values.

ligament formation. Although the fracture surfaces were not examined to the same degree as in the past, there is plenty of precedent for such ligament formation (Swadener et al., 1998 and 1999) at glass/epoxy interfaces. For the lower mode-mix phase angles ($-53^\circ < \psi < 30^\circ$), β_n and δ_{nc} are nearly constant, with average values of 14 and 2.5 μm, respectively. As a result, the normal TSR may be treated as independent of mode-mix over this range (TSR1 in Fig. 9). For higher mode-mix phase angles ($30^\circ < \psi < 90^\circ$), both β_n and δ_{nc} drop rapidly, leading to shorter interaction ranges and lower normal components of toughness.

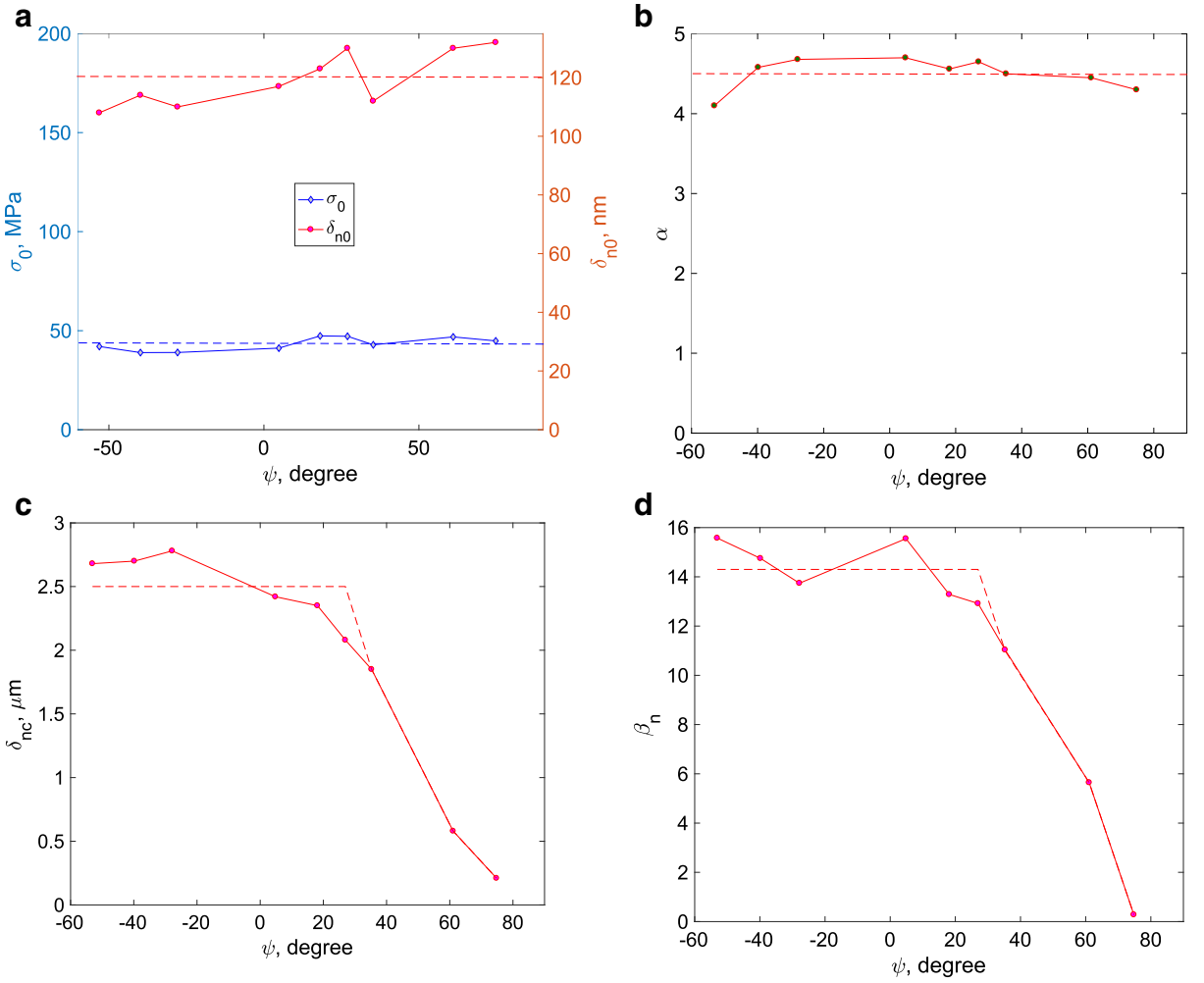

Fig. 10. Variation, over the range of mode-mixes considered, of the (a) strength and elastic range, (b) power-law exponent α, (c) interaction ranges and (d) descending power-law exponent of the normal traction–separation relations for tensile interactions between silicon and epoxy.

Table 2
Fitting parameters for the normal traction–separation relations.

ψ (°)	Γ_n (J/m^2)	σ_0(MPa)	δ_{n0} (nm)	α	β_n	δ_{nc}(nm)
−53.1	7.231	42.00	108	4.10	15.57	2680
−39.8	7.262	38.92	114	4.58	14.75	2700
−27.8	7.743	39.00	110	4.68	13.74	2780
4.8	6.420	41.17	117	4.70	15.55	2420
18.1	7.690	47.35	123	4.56	13.29	2350
27.0	7.510	47.14	130	4.65	12.92	2080
35.3	7.062	42.85	112	4.50	11.04	1850
61.1	4.291	46.84	130	4.45	5.64	580
74.8	3.853	44.84	132	4.30	0.28	210
Average	N/A	42.63	120	4.50	N/A	N/A

The shear traction–separation relations for all mode-mix phase angles are presented in Fig. 11. In all cases, the ascending parts were almost linear, albeit with slightly different slopes. The peak traction or the shear strength (τ_0) increased as the mode-mix increased. The peaks were followed by much sharper decays than were observed for the normal traction–separation relations, emphasizing that damage evolution was different under tension and shear. This is in contrast to most previous representations of mixed-mode traction–separation relations, where damage evolution is described by the same damage parameter for both tension and shear interactions.

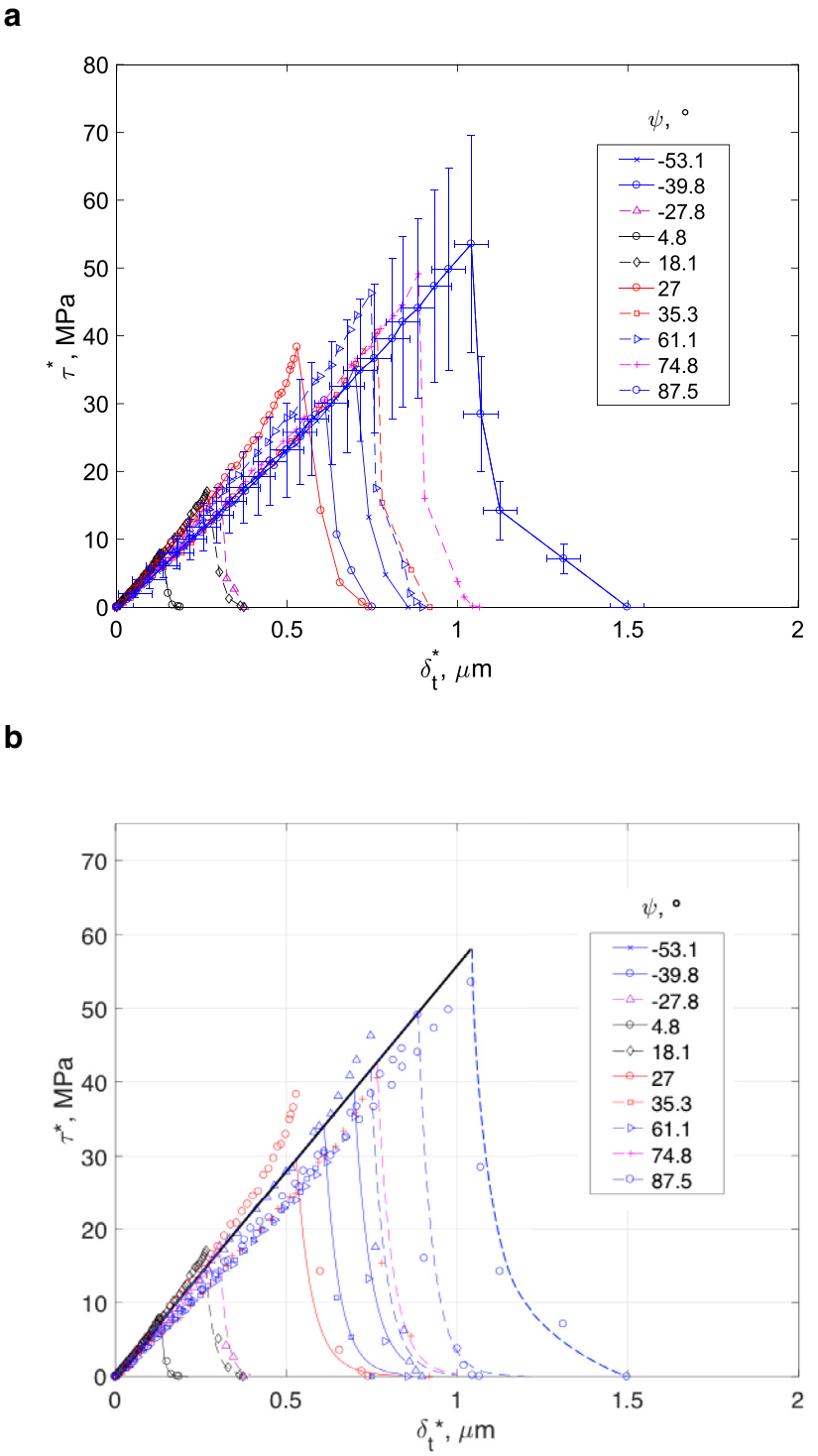

Fig. 11. Shear traction–separation relations for all mode-mix angles; (a) measurements only, (b) measurements (symbols) with fitting lines.

Each of the shear traction–separation relations was fit to a functional form with a linear ascending part followed by a power-law descending part, namely

$$\tau(\delta_t) = \begin{cases} k_t \delta_t, & 0 < \delta_t < \delta_{t0} \\ k_t \delta_{t0} \left(\frac{\delta_{tc} - \delta_t}{\delta_{tc} - \delta_{t0}} \right)^{\beta_t}, & \delta_{t0} < \delta_t < \delta_{tc} \end{cases}, \tag{22}$$

Table 3
Fitting parameters for the shear traction–separation relations.

ψ (°)	Γ_t (J/m^2)	k_t (MPa/μm)	δ_{t0} (nm)	β_t	δ_{tc} (nm)	$f_t = \delta_{t0}/\delta_{tc}$
−53.1	12.523	50.602	698	41.73	931	0.75
−39.8	8.353	52.354	610	33.20	772	0.79
−27.8	2.731	57.934	305	35.25	391	0.78
4.8	0.542	58.000	133	48.87	185	0.72
18.1	2.420	62.310	265	53.77	379	0.70
27.0	10.041	62.300	529	48.44	734	0.72
35.3	11.524	53.059	746	41.72	995	0.75
61.1	17.315	58.035	765	31.21	956	0.80
74.8	21.611	52.000	886	33.30	1122	0.79
87.5	30.511	51.462	1040	51.08	1465	0.71
Average	N/A	55.8	N/A	41.86	N/A	0.75

where k_t is the initial stiffness, δ_{t0} is the shear separation at the peak shear traction, δ_{tc} is the range of the shear interaction, and β_t is the power law exponent for the descending part. The fitting parameters of the extracted shear traction–separation relations are listed in Table 3 as a function of mode-mix. For the initial stiffness (k_t), there was no consistent trend with mode-mix and the variation appeared to be small. In fact, the average value of the initial stiffness is 55.8 MPa/μm, with a coefficient of variation of 8%. Consequently, the mean value may be used as the initial stiffness ($k_t = 55.8$ MPa/μm) for all the shear traction–separation relations. The separation δ_{t0} corresponds to damage initiation for the shear interactions, which increased with increasing mode-mix. The shear strengths were then recomputed from the measured δ_{t0} as $\tau_0 = k_t\delta_{t0}$, with $k_t = 55.8$ MPa/μm. The difference between the recomputed and original values was less than 8%.

Similar to the normal traction–separation relations, the two descending parameters, δ_{tc} and β_t, were determined by fitting both the shear traction–separation relations and the shear component of toughness (Fig. 8). Following Eqs. (15) and (22), the shear component of toughness is obtained as:

$$\Gamma_t = \int_0^{\delta_{tc}} \tau(\delta_t)d\delta_t = k_t\delta_{t0}^2\left[\frac{1}{2} + \frac{(f_t)^{-1} - 1}{\beta_t + 1}\right], \tag{23}$$

where $f_t = \delta_{t0}/\delta_{tc}$. The average value of β_t for all mode-mix values was 41.86 with a coefficient of variation of 2%, which describes a sharp descending stage of the shear traction. It was interesting to note that the ratio between δ_{t0} and δ_{tc} was nearly independent of mode-mix, with an average of 0.75 and a coefficient of variation of 5%. Thus, it is reasonable to take this ratio as a constant ($f_t = 0.75$) for all the shear traction–separation relations. Therefore, using the average values for k_t (55.8 MPa/μm), β_t (41.86), and f_t (0.75), the shear component of toughness is proportional to δ_{t0}^2, while both the shear strength τ_0 and the range of shear interaction δ_{tc} are proportional to δ_{t0} or $\sqrt{\Gamma_t}$. A comparison between the extracted shear traction–separation relations and the fitting embodied in Eqs. (22)–(23) revealed (Fig. 11b) that there was close agreement in both the ascending and descending portions of the shear traction–separation relations in all cases. Thus Eq. (22) provides a suitable representation for the shear traction–separation relations of the silicon/epoxy interface for all values of mode-mix between −53° and 87.5°.

4.3. Discussion

The extracted mixed-mode traction–separation relations are different from previous models that have been implemented for numerical simulations using commercial finite element packages such as ABAQUS. In order to conduct finite element analyses of the experimental configurations with the extracted traction–separation relations for the purposes of increasing insight and checking on internal consistency, a user-defined finite element subroutine (UEL) was programmed as a cohesive element within ABAQUS, following the approach by Rahul-Kumar et al. (1999), Song et al. (2008), and Alfano et al. (2007). The UEL formulation and implementation details are summarized in Appendix C.

The case that is considered in detail here is the symmetric ELS specimen, beginning with the stress contours at the peak force (Fig. 12a). At this moment, the cohesive zone had almost fully developed ahead of the initial crack tip when both the traction components became zero at the initial crack tip ($x = 0$) and the interfacial crack was about to grow in steady-state. The tractions along the interface ($x < 0$) ahead of the crack tip indicate the normal and shear interactions within the cohesive zone, which has a size of about 1000 μm. The maximum normal traction did not occur at the same location as that of the maximum shear traction. This is a consequence of the manner in which damage initiated and developed in the normal and shear interactions encoded in the implementation of the extracted traction–separation relations. The peak normal traction occurred ahead of the original crack tip by 650 μm whereas the peak shear traction was very close to the initial crack tip. Under pure mode I conditions, it is common to define the end of the cohesive zone as the location where the normal traction transitions from tension (positive) to compression (negative). If this idea is pursued here, then the end of the cohesive zone is co-located in tension and shear, in spite of the fact that the locations of the maximum tractions are not the same. The distributions of the normal and shear separations (Fig. 12b) in the cohesive zone are quite regular and do not suffer from any ambiguity.

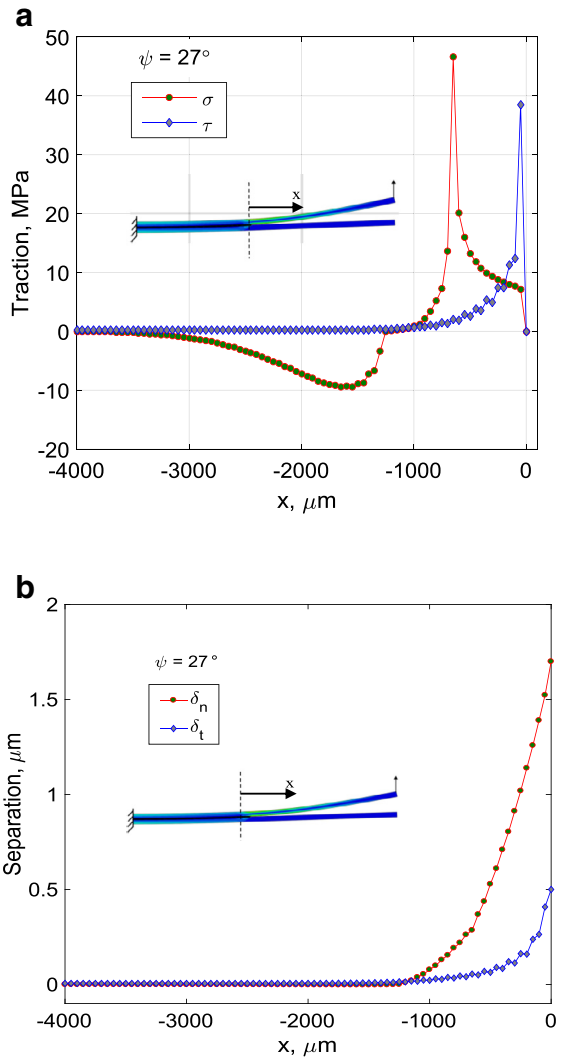

Fig. 12. (a) Traction and (b) separation distributions along the interface for an ELS specimen with silicon as the bottom adherend ($\psi = 27^{\circ}$), obtained from finite element simulation.

We compared the numerical solutions for force, end displacement and end rotation with measurements as a consistency check. Close agreement was found with these global quantities (Fig. 4a–c). We also compared the normal and shear CTODs (Fig. 4d) from the finite element solution with those obtained from the proposed deduction scheme (Eq. 10). The normal and shear components of the J-integral (Fig. 5) obtained from the finite element solution were also consistent with those based on measurements. From this favorable comparison of both far-field and local measurements, the proposed scheme for extracting traction–separation relations is considered to be validated. Nonetheless, a second, arguably stronger, validation analysis was conducted of the same loading condition with a completely different set of traction–separation relations (Wu et al., 2016), suitably interpolated for a mode-mix of 27°, as input for the properties of the interface. The data from the finite element solution was processed in the manner proposed in this paper. The input and extracted normal and shear components of the traction–separation relations were in excellent agreement (Fig. S16).

The paths that the crack tip displacements followed (δ_t^* versus δ_n^*) for a given mode-mix as the applied displacement was increased at a constant rate are shown in Fig. 13a. In all cases, the response was not proportional and the shear CTOD initially increased much more quickly than the normal component. At higher load levels and lower mode-mix angles ($< 27^{\circ}$), the steep rise in shear displacements transitioned to a plateau-like response where the normal components increased while the shear remained essentially constant. Such a transition did not develop for phase angles greater than 61.1°, where the shear CTOD was dominant. For phase angles of 27°, 18.1° and 4.8°, the plateau was followed by a faster increase in shear displacement. It did not appear to be possible to convert these observations into a unifying condition.

The paths followed in $J_{II} - J_I$ space are shown in Fig. 13b. For low phase angles, the paths were quite linear, all the way to the terminal state on each path corresponding to the steady state condition. The same was true for $\psi = 87.5^{\circ}$. In between these extremes, the responses were bilinear with the initial slope becoming steeper as the phase angles increased. In fact,

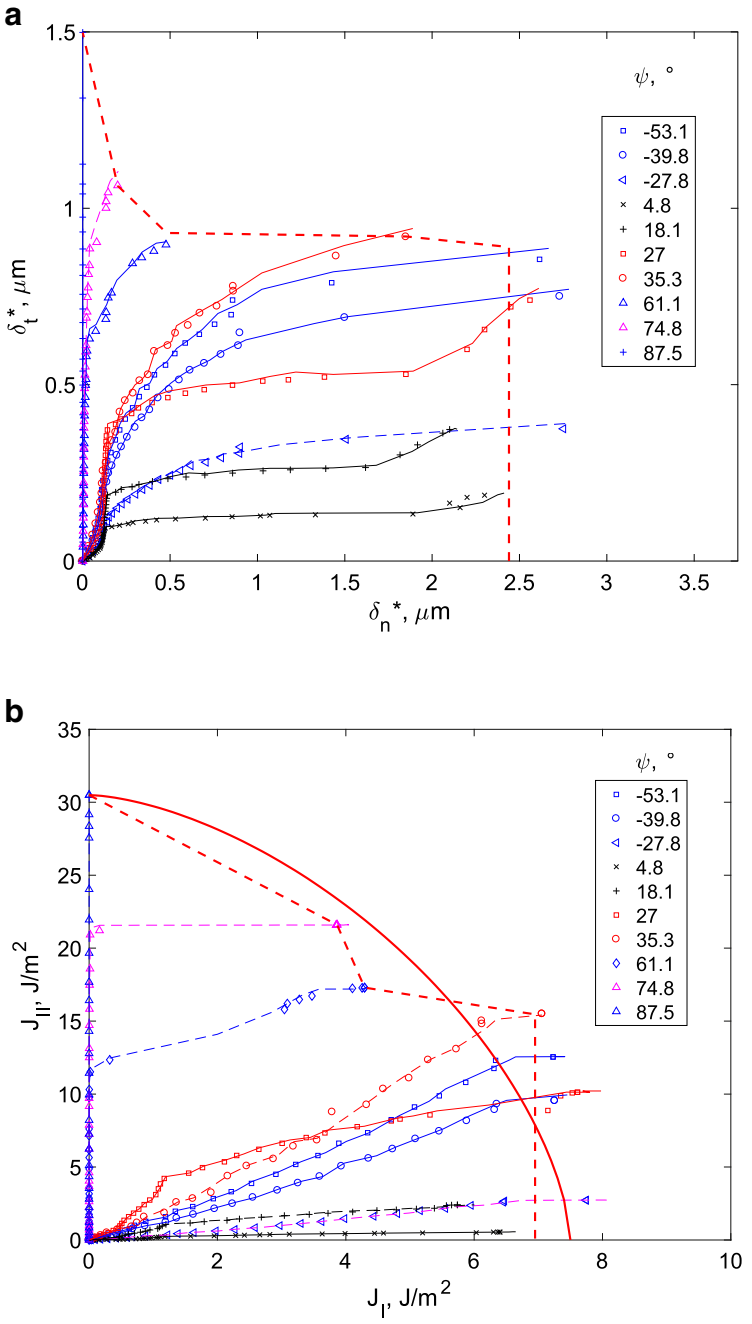

Fig. 13. Development of mode-mix in terms of (a) CTOD and (b) and J-integrals. In both cases, symbols represent the paths that were followed to failure, whose envelopes are approximately traced by the red dashed lines. The numerical results are shown in thin solid and dashed lines. The fitting with (Eq. 24) is shown as the thick solid line in (b). (For interpretation of the references to color in this figure legend, the reader is referred to the web version of this article.)

for $\psi \geq 61°$, the initial slope was essentially infinite. In these cases, the value of J_{II} at which the slope transitioned to a mode I dominant condition increased with increasing phase angle. The $J_{II} - J_I$ envelope for the transition to steady state followed the dashed red line. Again, it did not appear to be possible to convert these observations into a unifying condition. However, the relationship between the normalized J-integral components approximately followed the familiar form:

$$\left(\frac{J_I}{\Gamma_{nc}}\right)^{\lambda} + \left(\frac{J_{II}}{\Gamma_{tc}}\right)^{\lambda} = 1, \tag{24}$$

where $\lambda = 1.6$ provided the best fit with $\Gamma_{nc} = 7.3$ J/m^2 (which is the average value for $\psi \leq 30°$) and $\Gamma_{tc} = 30.5$ J/m^2 (which is the maximum shear toughness value for $\psi = 87.5°$), as illustrated by the red solid line in Fig. 13b.

The traction–separation relations extracted using the simple beam analysis ignored the presence of an epoxy layer between the two beams. As a result, the extracted separation includes the separation due to the deformation of the epoxy layer, leaving open the question as to how much of the extracted separation is due to the separation of the two interfaces and how much is due to the epoxy. In doing so, it is recognized that it is likely that a thin interphase layer forms in the epoxy next to the silicon. This interphase is expected (Sharpe, 1972) and has been shown to have mechanical and fracture behavior that differs from those of the bulk epoxy (Rakestraw et al., 1995). Thus it is possible that any extracted interfacial behavior could be attributed to that of the interphase region.

In developing the analysis to separate out the bulk and interfacial deformations, the contribution of the bulk behavior of the epoxy to the total separation was assumed to be elastic with a Young's modulus of 2 GPa and a Poisson's ratio of 0.35. The maximum normal traction was similar to the yield strength of the epoxy (Na et al., 2015), so any yielding in the epoxy is expected to be small, given the sharp decay in traction (Fig. 9). The contribution was determined by first conducting a finite element analysis of two silicon strips with the corresponding extracted traction–separation relation between them. At steady state growth, this analysis established the full extent of the cohesive zone and the distribution of the tractions acting over it. They were then applied to the top of a 50 μm-thick strip of epoxy (Fig. 14a), thereby matching the nominal thickness of the epoxy in the experiments. The bottom of the epoxy strip was fixed in both directions.

The applied traction profiles are shown in Fig. 14b. The resulting normal and shear deformations (δ_{ne}, δ_{te}) along the top surface of the epoxy layer are shown in Fig. 14c. As expected the maximum normal and tangential deformations in the epoxy coincided with the corresponding peak tractions. The interfacial separations were obtained by subtracting the epoxy deformations (Fig. 14c) from the distribution of extracted separations shown in Fig. 12b. The resulting traction–separation relations for the silicon/epoxy interface at a nominal mode-mix of 27° are shown in Fig. 15. After removing the elastic response of the epoxy layer in the cohesive zone, the ascending part of the normal traction–separation relation has a much higher stiffness. The initial normal separation (δ_{n0}) was reduced to 60 nm, which is about half the original value. The effect of the epoxy layer on the descending portion of the traction–separation relation becomes less noticeable as the traction drops. In the tangential direction, the linearly ascending portion of the response became slightly nonlinear as the traction reached its peak value. The shear interaction range dropped slightly from 0.78 to 0.74 μm, indicating that the shear deformation in the epoxy at this mode-mix was relatively minor. Similar behavior was found for all the other mode-mix phase angles (see Figs. S5–S13 in supplementary materials).

It has been shown (Sills and Thouless, 2013 and 2015) that, in laminated beam configurations under large-scale bridging conditions, the mode-mix in the cohesive zone varies as it develops. In the present study, large-scale bridging was indeed operative in that the steady state cohesive zone sizes were ~1 mm, many times larger than the 50 μm-thick epoxy layer. The crack tip displacements (Fig. 7a), J-integral components (Fig. 7b) and crack tip tractions (Fig. 7d), all followed nonlinear paths during the development of the cohesive zones. Thus the loading paths in laminated beam specimens under large-scale bridging conditions do not conform to the purely displacement or stress-controlled protocols considered by McGarry et al. (2014), who considered the consequences of developing traction–separation relations using potential or non-potential approaches. Nonetheless, the data obtained here for a silicon/epoxy interfaces does provide some insights, listed below, into the applicability of potential and non-potential approaches and on some experimental issues:

- The main difference between potential and non-potential approaches manifests in loading path-dependency (McGarry et al., 2014; Máirtín et al., 2014). Path independence is the hallmark of the potential-based approach. The traction–separation relations for the silicon/epoxy interface considered in this work exhibited significant loading path-dependency, thereby promoting the applicability of the non-potential approach for this interface, which typically incorporates the concept of damage development.
- For models based on damage development, a common damage function is usually assumed for both normal and shear traction–separation relations (Alfano and Crisfield, 2001; Alfano and Sacc, 2006; Camanho and Dávila, 2002). This avoids the possibility of negative energy dissipation under the assumption that the local mode-mix remains constant. However, different damage processes are clearly evident in the normal and shear traction–separation relations extracted here and the local mode-mix is far from being constant. Consequently, subsequent theoretical developments should be directed at accounting for such possibilities.
- For the silicon/epoxy interface considered here, the failure envelopes based either on crack tip displacements or J-integral components (Fig. 13) are more complex than the commonly assumed convex form. This is a reflection of the different forms of the traction–separation relations in tension and shear, the differences in their strengths and interaction ranges and the rates at which damage develops in each case. That said, it should be noted that the normal and shear tractions simultaneously dropped to zero at the initial crack tip as the cohesive zone became fully developed.
- While it may be possible, but nonetheless challenging, to exert local crack tip displacement control in biaxial loading configurations (Mello and Liechti, 2004), it will be a lot more challenging in laminated beam configurations, where the structure itself plays a role in the development of the cohesive zone and the local mode-mix. A complex control system would have to be developed to determine (δ_n^*, δ_t^*) from (Eqs. 11–12) using measurements of loads, load point displacements and rotations as well as crack length and then control them via feedback on the load point displacements (Δ_1, Δ_2).
- Using the balance condition to avoid coupling between the equations (Eqs. 8–9) governing normal and shear interactions has proven to be quite valuable in providing new insights into the development of cohesive zones under mixed-mode

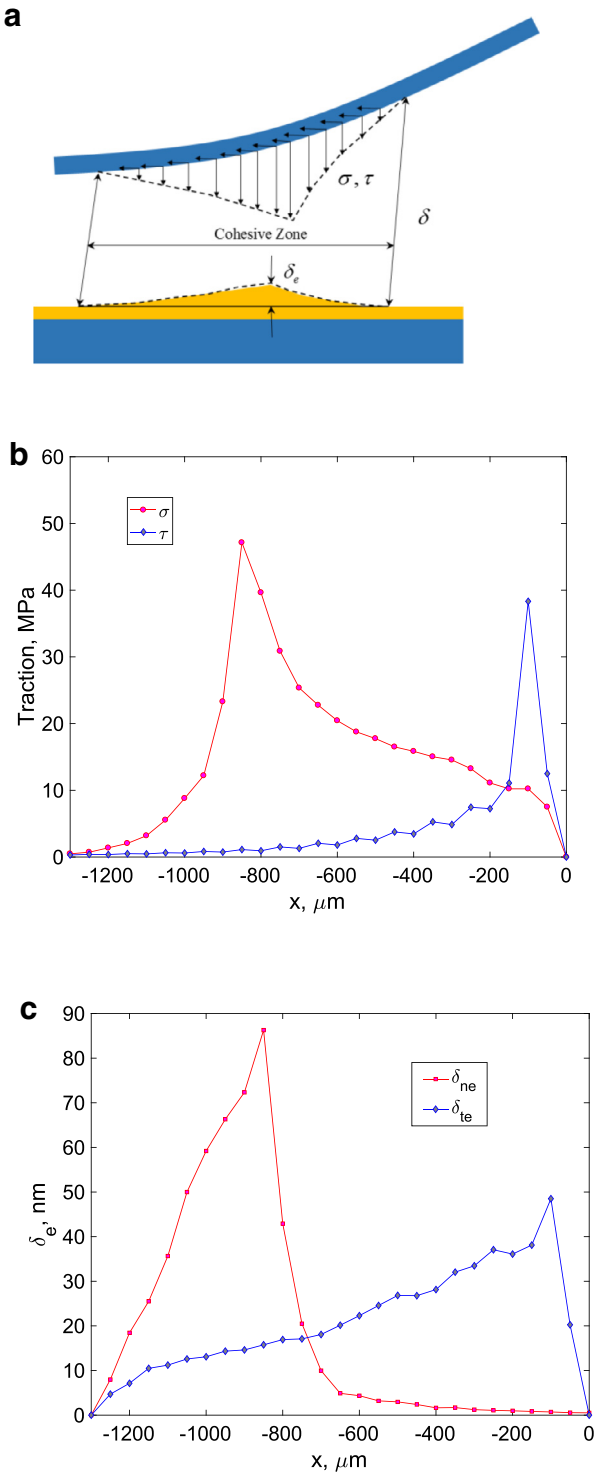

Fig. 14. Extracting the deformation of the epoxy in the cohesive zone. (a) Illustration of the reduced boundary value problem with (b) the tractions applied and (c) the surface displacement profiles of the epoxy layer ($\psi = 27^{\circ}$).

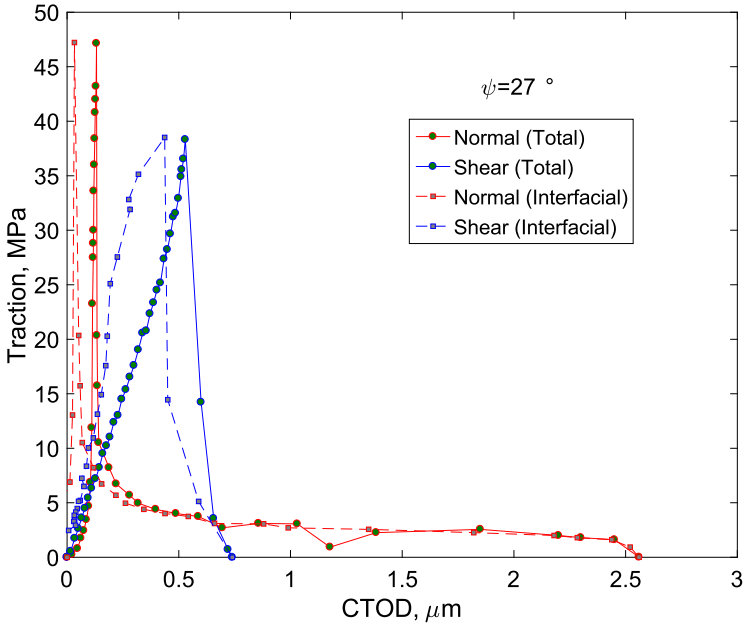

Fig. 15. Traction–separation relations at $\psi = 27^\circ$ before and after subtraction of the epoxy deformation.

loading. That is not to say that there was no coupling for this silicon/epoxy interface; the very fact that the extracted traction–separation relations depended on mode-mix indicates coupling and the approach proposed here appears to have been very effective in establishing it.

5. Conclusions

A simple beam analysis has been developed that accounts for the normal and shear interactions between the surfaces of two beams that have been brought into contact. The differential equations for the relative normal and tangential displacements between the interacting surfaces are generally coupled in the sense that the relative normal and shear displacements between the interacting surfaces each depend on both the normal and shear components of the traction between the two surfaces. The main thrust of this paper is that the coupling terms can be eliminated by making sure that the bending stiffness and height of the two beams satisfy the balance condition, $\frac{h_1}{D_1} = \frac{h_2}{D_2}$. It is further noted that, when this condition is satisfied, the normal and shear components of the J-integral and the crack tip displacement could be obtained from measurements of the remotely applied load and load point displacement and rotation of each beam. Then, taking derivative of each component of the J-integral with respect to its associated crack tip displacement simultaneously provided both normal and shear traction–separation relations at any value of the applied mode-mix.

The normal and shear traction–separation relations of a silicon/epoxy interface were obtained at ten different mode-mixes by making use of ELS and ENF specimens whose upper beam was always silicon. A variety of materials were used for the lower beam, with the thickness adjusted to satisfy the balance condition. This approach provided nominal mode-mix phase angles that ranged from -53° to 87.5°, as determined by linear elastic fracture mechanics (Hutchinson and Suo, 1992). Although the authors feel that it was beyond the scope of this study to investigate the issue of ambiguity in determining the mode-mix in laminated beams noted by others (Conroy et al., 2015), preliminary indications are that it does not arise when the balance condition is satisfied, even under large scale bridging.

The fracture toughness of the silicon/epoxy interface increased with increasing positive and negative shear component in accordance with previous results for epoxy interfaces with silicon, glass and sapphire. The normal component of the fracture toughness had an average value of $7.3 \pm 0.5\,\mathrm{J/m^2}$, for mode-mix phase angles below 35.3° and dropped to zero thereafter. Thus the increase in toughness with increasing shear was driven by the shear behavior of the interface with a maximum value of $30.5\,\mathrm{J/m^2}$ under nominally pure shear ($\psi = 87.5^\circ$). The normal and shear components of traction–separation relations were extracted at each mode-mix. In accordance with the fracture toughness result, the normal traction–separation relations were essentially the same for mode-mixes below 35.3°, with an average strength of 42.6 ± 3.8 MPa and interaction range of $2.4 \pm 0.3\,\mu$m. The damaging portion of the normal traction–separation relation followed a power law with an exponent of 14.3 ± 1.15. The shear traction–separation relations had an average stiffness of 55.8 ± 4.5 MPa/μm, with strengths varying from 7.7 MPa under approximately mode I conditions to 53.5 MPa at pure shear (mode II). The corresponding shear interaction ranges were 0.2 and 1.5 μm. The average power law exponent for the damaging portion of the traction–separation relations was 41.86.

The extracted separation values contained both the deformation of the epoxy and the silicon/epoxy interfaces. The former was estimated in a finite element analysis of a strip of epoxy with a nominal thickness of 50 μm that was subjected to the determined tractions acting over the length of a fully developed cohesive zone. The normal and shear strains in the bulk epoxy were less than 0.2%, so the behavior of the silicon/epoxy interface was similar to the extracted traction–separation relations except that the interface was stiffer in tension and shear. The strengths and interaction ranges remained the same.

The behavior of the silicon/epoxy interface that has been obtained in this study was compared with traction–separation relations derived from potential and damage based approaches. The basis of comparison was the paths followed in $J_{II}-J_I$, $\delta_t^*-\delta_n^*$ and $\tau^*-\sigma^*$ spaces. While the global mode-mix path was constant in each experiment, the paths followed in all three measures were nonlinear and varied from one mode-mix to another. This ruled out the applicability of traction–separation relations based on potentials because traction–separation relations based on potentials are independent of the loading path. Many damaged-based traction–separation relations assume that the normal and shear components have the same initial stiffness and damage behavior so that any differences in normal and shear traction–separation relations can only arise in the strength and interaction range. This was not the case for this silicon/epoxy interface, where the initial stiffness and damage evolution of the two components of the traction–separation relations were notably different. Furthermore, the failure envelopes in $J_{II}-J_I$ and $\delta_t^*-\delta_n^*$ spaces did not have the convex nature that has often been assumed. Although the comparison being made here is only based on the behavior of one interface, it is nonetheless hoped that the unique nature of the data will provide more food for thought in developing theoretical approaches that can accommodate some of the behavior that has been captured here.

Acknowledgments

The authors would like to acknowledge the contributions to the experimental work by Côme Pelée de Saint Maurice, a summer intern from École Polytechnique, Paris. The authors gratefully acknowledge partial financial support of this work by the National Science Foundation under Cooperative Agreement No. EEC-1160494. Any opinions, findings and conclusions or recommendations expressed in this material are those of the authors and do not necessarily reflect the views of the National Science Foundation.

Appendix A. A simple beam analysis

A.1. Constitutive relation

Assuming linearly elastic and isotropic constitutive relations in both the top and bottom beams, we have the force- and moment-displacement relationships as

$$N_i = A_i\frac{du_{i0}}{dx},\ M_i = D_i\frac{d^2w_i}{dx^2},\ A_i = \frac{E_ih_i}{1-\nu_i{}^2},\ D_i = \frac{E_ih_i{}^3}{12(1-\nu_i^2)}, \tag{A.1}$$

where, for each beam $(i=1,2)$, N_i and A_i are the axial force and stiffness, M_i and D_i are the bending moment and stiffness, ν_i and h_i are the Poisson's ratio and thickness.

A.2. Equilibrium equations

Considering an infinitesimal element for each beam as shown in Fig. 1b, the force and moment equilibrium requires that

$$\frac{dN_1}{dx} = \tau \text{ and } \frac{dN_2}{dx} = -\tau, \tag{A.2}$$

$$\frac{dQ_1}{dx} = -\sigma \text{ and } \frac{dQ_2}{dx} = \sigma, \tag{A.3}$$

$$\frac{dM_1}{dx} = Q_1 + \frac{h_1}{2}\tau \text{ and } \frac{dM_2}{dx} = Q_2 + \frac{h_2}{2}\tau, \tag{A.4}$$

where Q_i is the shear force acting on each beam element, and σ,τ are the normal and shear tractions along the interface between the two beams.

A.3. Governing equations for the interface

Taking the second and first derivatives of the relative normal and shear displacements in Eq. (3), respectively, we obtain the governing equations for the interface as follows:

$$\delta_n'' = w_1'' - w_2'' = \frac{M_1}{D_1} - \frac{M_2}{D_2}, \tag{A.5}$$

$$\delta_t' = \frac{N_1}{A_1} - \frac{N_2}{A_2} + \frac{h_1}{2D_1}M_1 + \frac{h_2}{2D_2}M_2. \tag{A.6}$$

The second derivative of δ_t can be obtained from Eq. (A.6) along with Eqs. (A.2) and (A.4), yielding

$$\delta_t'' - \left(\frac{h_1}{2D_1}Q_1 + \frac{h_2}{2D_2}Q_2\right) = \left(\frac{1}{A_1} + \frac{1}{A_2} + \frac{h_1^2}{4D_1} + \frac{h_2^2}{4D_2}\right)\tau. \tag{A.7}$$

For the laminated beam specimen, Eq. (A.3) can be integrated to obtain the shear forces in terms of the normal traction and the applied forces at the loading end, with which Eq. (A.7) becomes

$$\delta_t'' + \left(\frac{P_1h_1}{2D_1} + \frac{P_2h_2}{2D_2}\right) + \left(\frac{h_2}{2D_2} - \frac{h_1}{2D_1}\right)\int_0^x \sigma\, dx = \left(\frac{1}{A_1} + \frac{1}{A_2} + \frac{h_1^2}{4D_1} + \frac{h_2^2}{4D_2}\right)\tau. \tag{A.8}$$

By applying the balance condition, $\frac{h_1}{D_1} = \frac{h_2}{D_2}$, we eliminate the coupling with the normal traction in Eq. (A.8) so that

$$\delta_t'' + \frac{h_1}{2D_1}P = \left(\frac{1}{A_1} + \frac{1}{A_2} + \frac{h_1^2}{4D_1} + \frac{h_2^2}{4D_2}\right)\tau, \tag{A.9}$$

where $P = P_1 + P_2$.

Next, the fourth derivative of the normal separation δ_n can be obtained from Eq. (A.5) along with Eqs. (A.2–A.4) as

$$\delta_n{}^{(4)} = -\left(\frac{1}{D_1} + \frac{1}{D_2}\right)\sigma - \left(\frac{h_1}{2D_1} - \frac{h_2}{2D_2}\right)\tau'. \tag{A.10}$$

Again, when the condition $\frac{h_1}{D_1} = \frac{h_2}{D_2}$ is met, we eliminate the coupling with the shear traction in (A.10) and obtain the simple relationship

$$\sigma = -\hat{D}\delta_n{}^{(4)}, \tag{A.11}$$

where $\hat{D} \equiv (\frac{1}{D_1} + \frac{1}{D_2})^{-1}$. Therefore, the governing equations for the normal and shear interactions are decoupled in (A.9) and (A.11) under the balance condition, $\frac{h_1}{D_1} = \frac{h_2}{D_2}$.

A.4. Crack-tip displacements and J-integrals

To the right of the initial crack tip ($0 < x < a$), the shear traction is zero so that (Eq. A.9) can be integrated to obtain

$$\delta_t{}' = \frac{h_1}{2D_1}P(a - x). \tag{A.12}$$

Note that by (Eq. A.6) $\delta_t' = 0$ at $x = a$ because both the axial forces and bending moments are zero at the end of the beams. The first derivative of the shear displacement at the crack tip ($x = 0$) is then

$$\delta_t'^{*} = \frac{h_1}{2D_1}Pa. \tag{A.13}$$

Integrating (A.12), we obtain the relative shear displacement at the crack tip as

$$\delta_t^{*} = \delta_t(x = a) - \frac{Ph_1a^2}{4D_1}. \tag{A.14}$$

Since the axial forces are zero for $0 < x < a$, the relative shear displacement at the loading end of the beams is approximately, $\delta_t(x = a) \approx \frac{1}{2}(h_1\theta_1 + h_2\theta_2)$, where θ_1, θ_2 are the end-rotations of the top and bottom beams, respectively. The stretching is relatively small due to the limited shear interactions in the small cohesive zone. With this approximation, (Eq. 11) is obtained for the relative shear displacement at the crack tip. On the other hand, if the relative shear displacement at the loading end can be measured accurately, Eq. (A.14) should be used instead of Eq. (11). In the present study, $\delta_t(x = a)$ was not measured and (Eq. 11) was used as a reasonable approximation.

Similarly, to the right of the initial crack tip ($0 < x < a$), the governing equation for the relative normal displacement in (A.5) becomes

$$\delta_n'' = \left(\frac{P_1}{D_1} - \frac{P_2}{D_2}\right)(a - x), \tag{A.15}$$

which can be integrated to obtain the normal crack tip opening displacement as given in Eq. (10) and the derivatives

$$\delta_n'^{*} = \theta_1 - \theta_2 - \frac{a^2}{2}\left(\frac{P_1}{D_1} - \frac{P_2}{D_2}\right), \tag{A.16}$$

$$\delta_n^{*(2)} = a\left(\frac{P_1}{D_1} - \frac{P_2}{D_2}\right), \tag{A.17}$$

$$\delta_n{}^{*(3)} = -\left(\frac{P_1}{D_1} - \frac{P_2}{D_2}\right). \tag{A.18}$$

Therefore, by Eqs. (10) and (11), both the normal and tangential crack-tip displacements can be determined from the measurements at the loading ends of the beams including the loads (P_1 and P_2), displacements (Δ_1 and Δ_2) and rotations (θ_1 and θ_2). The derivatives in (A.13) and (A.16–A.18) are used to calculate the J-integral components as follows.

By Eq. (A.9), the shear traction in the cohesive zone ($x<0$) can be written as

$$\tau = \hat{A}\left[\delta_t{}'' + \frac{h_1}{2D_1}P\right], \tag{A.19}$$

where $\hat{A} \equiv (\frac{1}{A_1} + \frac{1}{A_2} + \frac{h_1^2}{4D_1} + \frac{h_2^2}{4D_2})^{-1}$. We calculate the shear component of the J-integral as

$$\begin{aligned} J_{\mathrm{II}} &= \int_0^{\delta_t^*} \tau\, d\delta_t = \hat{A}\int_0^{\delta_t^*}\left[\delta''_t + \frac{Ph_1}{2D_1}\right]d\delta_t \\ &= \hat{A}\int_0^{\delta_t^*}\left(\delta'_t\frac{\partial\delta'_t}{\partial\delta_t} + \frac{Ph_1}{2D_1}\right)d\delta_t \\ &= \frac{\hat{A}}{2}\left[\left(\delta_t^{*\prime}\right)^2 + \frac{Ph_1}{D_1}\delta_t^*\right], \end{aligned} \tag{A.20}$$

where we assume that both the shear displacement and its first derivative are zero at the clamped end ($x\to-\infty$). Substituting Eq. (A.13) and (11) into Eq. (A.20), we obtain a simplified expression for J_{II}, namely

$$J_{\mathrm{II}} = \frac{\hat{A}h_1}{4D_1}P(h_2\theta_2 + h_1\theta_1), \tag{A.21}$$

which is Eq. (13) in the main text.

Similarly, with Eq. (A.11), the normal component of the J-integral is calculated as

$$\begin{aligned} J_{\mathrm{I}} &= \int_0^{\delta_n^*}\sigma\, d\delta_n = -\hat{D}\int_0^{\delta_n^*}\delta_n{}^{(4)}d\delta_n \\ &= -\hat{D}\left\{\left[\delta_n{}^{(3)}\delta_n{}'\right]\Big|_{x=-\infty}^{x=0} - \int_0^{\delta_n^{*\prime}}\delta_n{}''\frac{\partial\delta_n{}''}{\partial\delta_n{}'}d\delta_n{}'\right\} \\ &= \hat{D}\left[\frac{1}{2}\left(\delta_n{}^{*(2)}\right)^2 - \delta_n^{*(3)}\delta_n^{*\prime}\right], \end{aligned} \tag{A.22}$$

where $\delta_n^{*\prime}$, $\delta_n^{*(2)}$ and $\delta_n^{*(3)}$ are the first, second, and third derivatives of the normal crack opening displacement at the initial crack tip ($x=0$). Again, we assume that the relative normal displacement and its derivatives are zero at the clamped end ($x\to-\infty$).

Substituting Eqs. (A.16–A.18) into Eq. (A.22), the normal component of the J-integral is obtained as

$$J_{\mathrm{I}} = \hat{D}\left(\frac{P_1}{D_1} - \frac{P_2}{D_2}\right)(\theta_1 - \theta_2), \tag{A.23}$$

which is Eq. (12) in the main text.

Appendix B. Parameters for nominal mode-mix

Following Hutchinson and Suo (1992), the parameters in Eq. (18) are defined and obtained as follows:

$$\alpha = \frac{\bar{E}_1 - \bar{E}_2}{\bar{E}_1 + \bar{E}_2},\ \beta = \frac{\bar{\nu}_2\bar{E}_1 - \bar{\nu}_1\bar{E}_2}{\bar{E}_1 + \bar{E}_2} \text{ with } \bar{E}_i = \frac{E_i}{1-\nu_i^2} \text{ and } \bar{\nu}_i = \frac{1-2\nu_i}{2(1-\nu_1)}$$

$$\varepsilon = \frac{1}{2\pi}\ln\left(\frac{1-\beta}{1+\beta}\right),\ \Sigma = \frac{1+\alpha}{1-\alpha}$$

$$\eta = h_1/h_2,\ \Delta = \left(1 + 2\Sigma\eta + \Sigma\eta^2\right)/[2\eta(1+\Sigma\eta)]$$

$$I = \Sigma\left[\left(\Delta - \eta^{-1}\right)^2 - \left(\Delta - \eta^{-1}\right) + 1/3\right] + (\Delta/\eta)\left(\Delta - \eta^{-1}\right) + \eta^{-3}/3$$

$$C_2 = \frac{\Sigma}{I}\left(\frac{1}{\eta} + \frac{1}{2} - \Delta\right),\ C_3 = \frac{\Sigma}{12I},$$

$$U = \left[1 + \Sigma\eta\left(4 + 6\eta + 3\eta^2\right)\right]^{-1},\ V = \left[12\left(1 + \Sigma\eta^3\right)\right]^{-1},$$

$$\gamma = \arcsin\left[6\sum \eta^2(1+\eta)\sqrt{UV}\right],$$

and the angle ω is a function of α, β and η, which was tabulated as in Suo and Hutchinson (1990). For the ELS specimens in the present study, we have $M_1 = M_3 = P_1 a$. For the ENF specimens, $M_1 = P_1 a$ and $M_3 = Pa$.

Appendix C. Cohesive element UEL implementation

The implementation of the cohesive elements requires the virtual work by the cohesive tractions along an interface and its first variation. This virtual work is

$$\delta W_{coh} = \int_{S_0} \{\delta\Delta\}^T \{T\} dS_0, \tag{C.1}$$

where S_0 is the interface in the undeformed configuration, $\{\delta\Delta\}$ is the virtual jump displacement across the cohesive element faces, and $\{T\}$ is the traction vector along the interface.

Discretization of the virtual displacement leads to

$$\delta W_{coh} = \{\delta u\}^T \int_{S_0} [N]^T \{T\} dS_0, \tag{C.2}$$

where $\{\delta u\}$ represents the virtual nodal displacements and $[N]$ is the nodal shape function matrix.

The first variation of the virtual work is

$$d(\delta W_{coh}) = \{\delta u\}^T \int_{S_0} [N]^T d\{T\} dS_0, \tag{C.3}$$

where the incremental tractions are related to the incremental nodal jump displacements as

$$d\{T\} = [C] d\{u\}. \tag{C.4}$$

Therefore, the first variation of virtual work can be obtained as

$$d(\delta W_{coh}) = \{\delta u\}^T [K] d\{u\}, \tag{C.5}$$

where $[K] = \int_{S_0} [N]^T [C][N] dS_0$ is the tangent stiffness matrix that is needed for Newton–Raphson iterations.

In a two-dimensional setting, the normal and shear tractions for each cohesive element are related to the nodal displacements by the traction–separation relations, and the corresponding Jacobian matrix is

$$[C] = \begin{bmatrix} \partial\sigma/\partial\delta_n & \partial\sigma/\partial\delta_t \\ \partial\tau/\partial\delta_n & \partial\tau/\partial\delta_t \end{bmatrix}. \tag{C.6}$$

For the experimental configurations in the present study, the normal and shear interactions are decoupled as a result of the balance condition. For each mode-mix, two traction–separation relations were extracted. A tabular input was used to import the extracted traction–separation relations for the UEL, where the normal traction was set to be independent of shear separation and vice versa. Therefore, the off-diagonal terms are zero in the Jacobian matrix. Given a set of separations (δ_n, δ_t) and the corresponding tractions (σ, τ), the derivatives in the Jacobian matrix are calculated by linear interpolation. It should be noted that the equivalent stiffness of the epoxy layer was used for the cohesive elements whenever the normal traction becomes compressive, i.e., $\frac{\partial\sigma}{\partial\delta_n}|_{\delta_n<0} = \frac{E_e}{h_e}$.

The UEL subroutine was integrated into ABAQUS in the form of a cohesive element. The nodes in the UEL elements were directly tied to those of the adjacent elements in the finite element model. A two-integration-point scheme was used where the traction was calculated based on the openings given the tabulated input. The global field equations were solved incorporating both the UEL elements and others in the model. A typical stress distribution near the crack tip is presented in Figs. S3 and S4.

We note that the current UEL implementation is specific to the experimental configurations in the present study, without explicit coupling between the normal and shear interactions. The fact that the traction–separation relations depend on the mode-mix indicates that they are coupled, but we do not have a general formulation for coupled interactions. Instead, the traction–separation relations extracted for each mode-mix were imported in the finite element analysis of the same experimental configuration, for the purpose of consistency checking. It is also assumed that both the normal and shear separations increased monotonically in the cohesive elements so that no damage parameters are needed.

Supplementary material

Supplementary material associated with this article can be found, in the online version, at doi:10.1016/j.jmps.2018.12.004.

References

Alfano, G., Crisfield, M.A., 2001. Finite element interface models for the delamination analysis of laminated composites: mechanical and computational issues. Int. J. Num. Methods Eng. 50, 1701–1736.

Alfano, G., Sacco, E., 2006. Combining interface damage and friction in a cohesive-zone model. Int. J. Numer. Methods Eng. 68, 542–582.

Alfano, M., Furgiuele, F., Leonardi, A., Maletta, C., Paulino, G.H., 2007. Cohesive zone modeling of mode-I fracture in adhesive bonded joints. Key Eng. Mater. 348, 13–16.

Andersson, T., Stigh, U., 2004. The stress–elongation relation for an adhesive layer loaded in peel using equilibrium of energetic forces. Int. J. Solids Struct. 41 (2), 413–434.

Barenblatt, G.I., 1962. The mathematical theory of equilibrium cracks in brittle fracture. Adv. Appl. Mech. 7, 55–129.

Bing, Q., Davidson, B.D., 2010. An improved methodology for measuring the interfacial toughness of sandwich beams. In: Daniels, I.M., Gdoutos, E.E., Rajapakse, Y.D.S. (Eds.), In Major Accomplishments in Composite Materials and Sandwich Structures: An Anthology of ONR Sponsored Research. Springer, pp. 365–380.

Cao, Z., Tao, L., Akinwande, D., Huang, R., Liechti, K.M., 2016. Mixed-mode traction–separation relations between graphene and copper by blister tests. Int. J. Solids Struct. 84, 147–159.

Camanho, P., Dávila, C., 2002. Mixed-mode decohesion finite elements for the simulation of delamination in composite materials, NASA/TM-2002-211737.

Carlson, A., Kim-Lee, H.-J., Wu, J., Elvikis, P., Cheng, H., Kovalsky, A., Elgan, S., Yu, Q., Ferreira, P.M., Huang, Y., Turner, K.T., Rogers, J.A., 2011. Shear-enhanced adhesiveless transfer printing for use in deterministic materials assembly. Appl. Phys. Lett. 98 (26), 264104.

Chai, Y.S., Liechti, K.M., 1992. Asymmetric shielding in interfacial fracture under in-plane shear. J. Appl. Mech. 59 (2), 295–304.

Charalambides, P.G., Cao, H.C., Lund, J., Evans, A.G., 1990. Development of a test specimen for measuring the mixed mode fracture resistance of bimaterial interfaces. Mech. Mater. 8, 269–283.

Charalambides, P.G., Lund, J., Evans, A.G., McMeeking, R.M., 1989. A test specimen for determining the fracture resistance of bimaterial interfaces. J. Appl. Mech. 56, 77–82.

Charalambides, P.G., Kinloch, AJ., Wang, Y., Williams, J.G., 1992. On the analysis of mixed mode failure. Int. J. Fract. 54, 269–291.

Chow, C.L., Woo, C.W., Sykes, J.L., 1979. On the determination and application of COD to epoxy-bonded aluminum joints. J. Strain Anal. Eng. Des. 14 (2), 37–42.

Conroy, M., Kinloch, A.J., Williams, J.G., Ivankovic, A., 2015. Mixed mode partitioning of beam-like geometries: a damage dependent solution. Eng. Fract. Mech. 149, 351–367.

Cox, B.N., Marshall, D.B., 1991. The determination of crack bridging forces. Int. J. Fract. 49 (3), 159–176.

Davidson, B., Gharibian, S.J., Yu, L., 1997. Evaluation of energy release rate-based approaches for predicting delamination growth in laminated composites. Int. J. Fract. 105, 343–365.

Dollhofer, J., Beckert, W., Lauke, B., Schneider, K., 2000. Fracture mechancial charaterization of mixed-mode toughness of thermoplasti/glass interfaces. Comput. Mater. Sci. 19, 223–228.

Dugdale, D.S., 1960. Yielding of steel sheets containing slits. J. Mech. Phys. Solids 8 (2), 100–104.

Feraren, P., Jensen, H.M., 2004. Cohesive zone modeling of interface fracture near flaws in adhesive joints. Eng. Fract. Mech. 71 (15), 2125–2142.

Fernlund, G., Spelt, J.K., 1994. Mixed-mode fracture characterization of adhesive joints. Compos. Sci. Technol. 50, 441–449.

Gain, A.L., Carroll, J., Paulino, G.H., Lambros, J., 2011. A hybrid experimental/numerical technique to extract cohesive fracture properties for mode-I fracture of quasi-brittle materials. Int. J. Fract. 169 (2), 113–131.

Gowrishankar, S., Mei, H., Liechi, K.M., Huang, R., 2012. A comparison of direct and iterative methods for determining traction–separation relations. Int. J. Fract. 177 (2), 109–128.

Guo, Z.K., Kobayashi, A.S., Hay, J.C., White, K.W., 1999. Fracture process zone modeling of monolithic Al_2O_3. Eng. Fract. Mech. 63 (2), 115–129.

Ho, P.S., Wang, G., Ding, M., Zhao, J.-H., Dai, X., 2004. Reliability issues for flip-chip packages. Microelectron. Reliab. 44, 719–737.

Högberg, J.L., Sørensen, B.F., Stigh, U., 2007. Constitutive behaviour of mixed mode loaded adhesive layer. Int. J. Solids Struct. 44 (25-26), 8335–8354.

Hong, S., Kim, K.-S., 2003. Extraction of cohesive-zone laws from elastic far-fields of a cohesive crack tip: a field projection method. J. Mech. Phys. Solids 51, 1267–1286.

Hutchinson, J.W., Suo, Z., 1992. Mixed mode cracking in layered materials. Adv. Appl. Mech. 29, 64–191.

Ji, G., Ouyang, Z., Li, G., 2012. On the interfacial constitutive laws of mixed mode fracture with various adhesive thicknesses. Mech. Mater. 47, 24–32.

Kanninen, M.F., 1973. An augmented double cantilever beam model for studying crack propagation and arrest. Int. J. Fract. 9 (1), 83–92.

Kim, H.G., Chew, H.B., Kim, K.S., 2012. Inverse extraction of cohesive zone laws by field projection method using numerical auxiliary fields. Int. J. Numer. Methods Eng. 91 (5), 516–530.

Kim-Lee, H.-J., Carlson, A., Grierson, D.S., Rogers, J.A., Turner, K.T., 2014. Interface mechanics of adhesiveless microtransfer printing processes. J. Appl. Phys. 115 (14), 143513.

Kysar, J.W., 2001. Crack-opening interferometry at interfaces of transparent materials and metals. Exp. Mech. 41 (1), 52–57.

Li, G., Ouyang, Z., Li, G., Ibekwe, S., Pang, S-S., 2010. Effects of adhesive thickness on global and local Mode-I interfacial fracture of bonded joints. Int. J. Solids Struct. 47, 2445–2458.

Li, S., Thouless, M.D., Wass, A.M., Schroeder, J.A., Zavattieri, P.D., 2005. Use of mode-I cohesive-zone models to describe the fracture of an adhesively-bonded polymer-matrix composite. Compos. Sci. Technol. 65 (2), 281–293.

Li, S., Thouless, M.D., Wass, A.M., Schroeder, J.A., Zavattieri, P.D., 2006. Mixed-mode cohesive-zone models for fracture of an adhesively bonded polymer–matrix composite. Eng. Fract. Mech. 73 (1), 64–78.

Liang, Y.-M., Liechti, K.M., 1995. Toughening mechanisms in mixed-mode interfacial fracture. Int. J. Solids Struct. 32 (6-7), 957–978.

Liechti, K.M., 1993. On the use of classical interferometry techniques in fracture mechanics. In: Epstein, J.S. (Ed.), Experimental Techniques in Fracture, III. VCH Publishers, New York, pp. 95–124.

Liechti, K.M., Na, S.R., Seitz, O., Chabal, Y., 2013. A high vacuum fracture experiment for examining molecular interactions. Exp. Mech. 53, 231–241.

Liu, X.H., Lane, M.W., Shaw, T.M., Simonyi, E., 2007. Delamination in patterned films. Int. J. Solids Struct. 44, 1706–1718.

Máirtín, É.Ó., Parry, G., Beltz, G.E., McGarry, J.P., 2014. Potential-based and non-potential-based cohesive zone formulations under mixed-mode separation and over-closure–Part II: finite element applications. J. Mech. Phys. Solids 63, 363–385.

Mangalgiri, P.D., Johnson, W.S., R.A. Everett Jr., 1986. Effect of adherend thickness and mixed-mode loading on debond growth in adhesively bonded composite joints. NASA TM-88992: 1–46.

McGarry, J.P., Éamonn, Ó.M., Guillaume, P., Beltz, G.E., 2014. Potential-based and non-potential-based cohesive zone formuatlinos under mixed-mode separation and over-closure. Part I: theoretical analysis. J. Mech. Phys. Solids 63, 336–362.

Mello, A.W., Liechti, K.M., 2006. The effect of self-assembled monolayers on interfacial fracture. J. Appl. Mech. 73 (5), 860–870.

Mello, A.W., Liechti, K.M., 2004. A piezoelectric biaxial loading device for interfacial fracture experiments. Exp. Mech. 44 (5), 495–501.

Mohammed, I., Liechti, K.M., 2000. Cohesive zone modeling of crack nucleation at bimaterial corners. J. Mech. Phys. Solids 48, 735–764.

Moroni, F., Pirondi, A., 2011. Cohesive zone model simulation of fatigue debonding along interfaces. Proc. Eng. 10, 1829–1834.

Na, S.R., Sarceno, D.A., Liechti, K.M., 2016. Ultra long-range interactions between silicon surfaces. Int. J. Solids Struct. 80, 168–180.
Na, S.R., Suk, J.W., Tao, L., Akinwande, D., Ruoff, R.S., Huang, R., Liechti, K.M., 2015. Selective mechanical transfer of graphene from seed copper foil using rate effects. ACS Nano 9 (2), 1325–1335.
Needleman, A., 1987. A continuum model for void nucleation by inclusion debonding. J. Appl. Mech. 54, 525–531.
Nguyen, C., Levy, A.J., 2009. An exact theory of interfacial debonding in layered elastic compsosites. Int. J. Solid Struct. 46, 2712–2723.
Ouyang, Z., Li, G., 2009. Nonlinear interface shear fracture of end notched flexure specimens. Int. J. Solids Struct. 46, 2659–2668.
Pan, B., Qian, K., Xie, H., Asundi, A., 2009. Two-dimensional digital image correlation for in-plane displacement and strain measurement: a review. Meas. Sci. Technol. 20 (6), 1–17.
Park, K., Paulino, G.H., Roesler, J., 2009. A unified potential-based cohesive model of mixed-mode fracture. J. Mech. Phys. Solids 57 (6), 891–908.
Parmigiani, J.P., Thouless, M.D., 2007. The effects of cohesive strength and toughness on mixed-mode delamination of beam-like geometries. Eng. Fract. Mech. 74, 2675–2699.
Pronin, A.N., Gupta, V., 1998. Measurement of thin film interface toughness by using laser-generated stress pulses. J. Mech. Phys. Solids 46 (3), 389–410.
Rakestraw, M.D., Taylor, M.W., Dillard, D.A., Chang, T., 1995. Time dependent crack growth and loading rate effects on interfacial and cohesive fracture of adhesive joints. J. Adhes. 55 (1-2), 123–149.
Rahul-Kumar, P., et al., 1999. Polymer interfacial fracture simulations using cohesive elements. Acta Materialia 47 (15-16), 4161–4169.
Rahulkumar, P., Jagota, A., Bennison, S.J., Saigal, S., 2000. Cohesive element modeling of viscoelastic fracture: application to peel testing of polymers. Int. J. Solids Struct. 37, 1873–1897.
Reeder, J.R., Crews Jr., J.R., 1990. Mixed-mode bending method for delamination testing. AIAA J. 28 (7), 1270–1276.
Sharpe, L.H., 1972. The interphase in adhesion. J Adhes. 4 (1), 51–64.
Shen, B., Paulino, G.H., 2011. Direct extraction of cohesive fracture properties from digital image correlation: a hybrid inverse technique. Exp. Mech. 51 (2), 143–163.
Shirani, A., Liechti, K.M., 1998. A calibrated fracture process zone model for thin film blistering. Int. J. Fract. 93, 281–314.
Sills, R.B., Thouless, M.D., 2013. The effect of cohesive-law parameters on mixed-mode fracture. Eng. Fract. Mech. 109, 353–368.
Sills, R.B., Thouless, M.D., 2015. Cohesive-length scales for damage and toughening mechanisms. Int. J. Solids Struct. 55, 32–43.
Sokolnikoff, I.S., 1946. Mathematical Theory of Elasticity. McGraw-Hill, New York.
Song, S.H., Paulino, G.H., Buttlar, W.G., 2008. Influence of the cohesive zone model shape parameter on asphalt concrete fracture behavior. In: Proceedings of the AIP Conference, 973, pp. 730–735.
Sørensen, B.F., Jacobsen, T.K., 2003. Determination of cohesive laws by the J integral approach. Eng. Fract. Mech. 70 (14), 1841–1858.
Sørensen, B.F., Kirkegaard, P., 2006. Determination of mixed mode cohesive laws. Eng. Fract. Mech. 73 (17), 2642–2661.
Sørensen, B.F., Jørgensen, K., Jacobsen, T.K., Østergaard, R.C., 2006. DCB-specimen loaded with uneven bending moments. Int. J. Fract. 141 (1-2), 163–176.
Sorensen, L., Botsis, J., Gmür, Th., Humbert, L., 2008. Bridging tractions in mode I delamination: measurements and simulations. Compos. Sci. Technol. 68 (12), 2350–2358.
Stigh, U., Andersson, T., 2000. An experimental method to determine the complete stress-elongation relation for a structureal adhesive layer loaded in peel. In: Williams, J.G., Pavan, A. (Eds.), Fracture of Polymers, Composites and Adhesives, vol. 27. European Structural Integrity Society, pp. 297–306.
Sundararaman, V., Davidson, B.D., 1997. An unsymmetric double cantilever beam test for interfacial fracture toughness determination. Int. J. Solids Struct. 34 (7), 799–817.
Suo, Z., Hutchinson, J.W., 1990. Interface crack between two elastic layers. Int. J. Fract. 43 (1), 1–18.
Swadener, J.G., Liechti, K.M., 1998. Asymmetric shielding mechanisms in the mixed-mode fracture of a glass/epoxy interface. J. Appl. Mech. 65 (1), 25–29.
Swadener, J.G., Liechti, K.M., de Lozanne, A.I., 1999. The intrinsic toughness and adhesion mechanisms of a glass/epoxy interface. J. Mech. Phys. Solids 47 (2), 223–258.
Tvergaard, V., Hutchinson, J.W., 1996. On the toughness of ductile adhesive joints. J. Mech. Phys. Solids 44 (5), 789–800.
Ungsuwarungsru, T., Knauss, W.G., 1987. The role of damage-softened material behavior in the fracture of composites and adhesive. Int. J. Fract. 35, 221–241.
Valoroso, N., Champaney, L., 2006. A damage-mechanics-based approach for modelling decohesion in adhesively bonded assemblies. Eng. Fract. Mech. 73 (18), 2774–2801.
Wang, H., Vukanh, T., 1996. Use of end-loaded-split (ELS) test to study stable fracture behavior of composites under mode-II loading. Compos. Struct. 36, 71–79.
Wang, S., Harvey, C.M., Guan, L., 2013. Partition of mixed modes in layered isotropic double cantilever beams with non-rigid cohesive interfaces. Eng. Fract. Mech. 111, 1–25.
Warrior, N.A., Pickett, A.K., Lourenco, N.S.F., 2003. Mixed-mode delamination experimental and numerical studies. Strain 39, 153–159.
Williams, J.G., 1988. On the calculation of energy release rates for cracked laminates. Int. J. Fracture 36 (2), 101–119.
Williams, J.G., 1989. End corrections for orthotropic DCB specimens. Compos. Sci. Technol. 35 (4), 367–376.
Wu, C., Gowrishankar, S., Huang, R., Liechti, K.M., 2016. On determining mixed-mode traction–separation relations for interfaces. Int. J. Fract. 202, 1–19.
Wu, C., 2016. Using Far-Field Measurements for Determining Mixed-Mode Interactions at Interfaces. PhD Dissertation. University of Texas at Austin.
Xin, H., Borduin, R., Jiang, W., Liechti, K.M., Li, W., 2017. Adhesion energy of as-grown graphene on copper foil with a blister test. Carbon 123, 243–249.
Xu, X-P., Needleman, A., 1993. Void nucleation by inclusion debonding in a crystal matrix. Model. Simul. Mater. Sci. Eng. 2, 417–418.
Yang, Q.D., Thouless, M.D., 2001. Mixed-mode fracture analyses of plastically-deforming adhesive joints. Int. J. Fract. 110 (2), 175–187.
Yuan, H., Chen, J., 2003. Computational analysis of thin coating layer failure using a cohesive model and gradient plasticity. Eng. Fract. Mech. 70, 1929–1942.
Zavattieri, P.D., Hector Jr, L.G., Bower, A.F., 2008. Cohesive zone simulations of crack growth along a rough interface between two elastic–plastic solids. Eng. Fract. Mech. 75, 4309–4332.
Zhang, X., Im, S.H., Huang, R., Ho, P.S., 2008. Chip-packaging interaction and reliability impact on Cu/Low-k interconnects. In: Integrated Interconnect Technologies for 3D Nanoelectronic Systems. Artech House, Norwood, pp. 23–59.
Zhu, Y., Liechti, K.M., Ravi-Chandar, K., 2009. Direct extraction of rate-dependent traction–separation laws for polyurea/steel interfaces. Int. J. Solids Struct. 46 (1), 31–51.